De novo VPS4A mutations cause multisystem disease with abnormal neurodevelopment

Catherine Rodger,[1,2,25] Elisabetta Flex,[3,25] Rachel J. Allison,[1,2,25] Alba Sanchis-Juan,[4,5,25]

Marcia A Hasenahuer,[2,6] Serena Cecchetti,[7] Courtney E. French,[2] James R. Edgar,[1,8]

Giovanna Carpentieri,[3,9] Andrea Ciolfi,[9] Francesca Pantaleoni,[9] Alessandro Bruselles,[3]

Genomics England Research Consortium,[10] Roberta Onesimo,[11] Giuseppe Zampino,[11,12]

Francesca Marcon,[13] Ester Siniscalchi,[13] Melissa Lees,[14] Deepa Krishnakumar,[15] Emma

McCann,[16] Dragana Yosifova,[17] Joanna Jarvis,[18] Michael C. Kruer,[19] Warren Marks,[20]

Jonathan Campbell,[21] Louise E. Allen,[22] Stefano Gustincich,[23,24] F Lucy Raymond,[1,2,26]

Marco Tartaglia,[9,26]* and Evan Reid[1,2,26]**

1. Cambridge Institute for Medical Research, University of Cambridge, Cambridge, CB2 0XY, UK.

2. Department of Medical Genetics, University of Cambridge, Cambridge, CB2 0QQ, UK.

3. Department of Oncology and Molecular Medicine, Istituto Superiore di Sanità, Rome, 00161, Italy

4. Department of Haematology, NHS Blood and Transplant Centre, University of Cambridge, Cambridge, CB2 0XY, UK

5. NIHR BioResource, Cambridge University Hospitals NHS Foundation Trust, Cambridge Biomedical Campus, CB2 0QQ, Cambridge, UK

6. European Molecular Biology Laboratory – European Bioinformatics Institute (EMBL-EBI), Wellcome Genome Campus, Hinxton, Cambridgeshire, CB10 1SA, UK

7. Microscopy Area, Core Facilities, Istituto Superiore di Sanità, Rome, 00161, Italy

8. Department of Pathology, University of Cambridge, CB2 1QP, UK

9. Genetics and Rare Diseases Research Division, Ospedale Pediatrico Bambino Gesù, IRCCS, Rome, 00146, Italy

10. Genomics England, London UK

11. Fondazione Policlinico Universitario A. Gemelli -IRCCS, Rome, 00168, Italy

12. Università Cattolica del Sacro Cuore, Rome, 00168, Italy

13. Unit of Mechanisms, Biomarkers and Models, Department of Environment and Health, Istituto Superiore di Sanità, Rome, 00161, Italy

14. Department of Clinical Genetics, Great Ormond Street Hospital, London, WC1N 3JH, UK

15. Department of Paediatric Neurology, Cambridge University Hospitals NHS Foundation Trust, Cambridge, CB2 0QQ, UK

16. Department of Clinical Genetics, Liverpool Women's Hospital, Liverpool, L8 7SS, UK

17. Department of Medical Genetics, Guys' and St Thomas' NHS Foundation Trust, London, SE1 9RT, UK

18. Clinical Genetics, Birmingham Women's and Children's NHS Foundation Trust, Birmingham, B15 2TG, UK.

19. Phoenix Children's Hospital, Phoenix, Arizona, 76109, USA

20. Cook Children's Medical Centre, Fort Worth, Texas, 76104, USA

21. Colchester Hospital, East Suffolk and North Essex NHS Foundation Trust, Essex, CO4 5JL, UK

22. Ophthalmology Department, Cambridge University Hospitals NHS Foundation Trust, Cambridge, CB2 0QQ, UK

23. Department of Neuroscience and Brain Technologies, Istituto Italiano di Tecnologia, Genova, 16163, Italy.

24. Area of Neuroscience, SISSA, Trieste, 34136, Italy.

25. These authors contributed equally to this work

26. These authors contributed equally to this work

Correspondence:

* Email: marco.tartaglia@opbg.net

** Email: ealr4@cam.ac.uk

Abstract

The endosomal sorting complexes required for transport (ESCRTs) are essential for multiple membrane modelling and membrane-independent cellular processes. Here we describe 6 unrelated individuals with *de novo* missense variants affecting the ATPase domain of VPS4A, a critical enzyme regulating ESCRT function. Probands had structural brain abnormalities, severe neurodevelopmental delay, cataracts, growth impairment and anaemia. In cultured cells, over-expression of VPS4A mutants caused enlarged endosomal vacuoles resembling those induced by expression of known dominant-negative ATPase-defective forms of VPS4A. Proband-derived fibroblasts had enlarged endosomal structures with abnormal accumulation of the ESCRT protein IST1 on the limiting membrane. VPS4A function was also required for normal endosomal morphology and IST1 localisation in iPSC-derived human neurons. Mutations affected other ESCRT-dependent cellular processes, including regulation of centrosome number, primary cilium morphology, nuclear membrane morphology, chromosome segregation, mitotic spindle formation and cell cycle progression. We thus characterize a distinct multisystem disorder caused by mutations affecting *VPS4A*, and demonstrate that its normal function is required for multiple human developmental and cellular processes.

Introduction

The endosomal sorting complexes required for transport (ESCRTs) are multifunctional membrane modelling machineries that drive membrane fission or constriction in cellular processes that involve "inside out" membrane topology.[1-3] These are exemplified by fission reactions that cause vesicle budding away from the cytoplasm, in which ESCRT-III complexes assemble on the inner cytosolic face of a vesicle neck and promote membrane constriction from the inside. Modification of ESCRT-III complexes drives fission, and this is performed by the catalytic activity of members of the VPS4 ATPase family (which in vertebrates comprises two paralogues, VPS4A and VPS4B) – thus VPS4 is an indispensable component of all ESCRT-related membrane modelling.[4] Processes that involve this type of membrane topology include formation of the late endosomal multivesicular body (MVB), nuclear envelope reformation and the abscission stage of cell division, amongst others.[1-3] In addition, certain ESCRT-III-associated proteins are active in more conventional "outside in" fission, notably in endosomal tubule fission, where atypical ESCRT-III proteins constrict from the outside to promote fission of sorting tubules from the endosomal body.[5; 6]

Study of the ESCRT complexes and VPS4 in the endocytic pathway has informed mechanistic understanding of their role in membrane modelling.[2; 3; 7-9] Endocytosis regulates the cell surface concentration of plasma membrane proteins and so controls multiple critical cellular processes. After endocytosis from the cell surface, membrane proteins are trafficked to the early sorting endosome, from where they may be sorted away from the endosomal system (e.g. to the plasma membrane) or retained for degradation in the late endosome-lysosome pathway.[10] Membrane proteins to be degraded are exposed to the lumenal degradative compartment of the late endosome and lysosome by a process involving inward budding of the endosomal limiting membrane to form the intralumenal vesicles (ILVs) of the late endosome or multivesicular body (MVB). Concentration and sorting of cargoes into, and

formation of, the ILVs is accomplished by the action of the ESCRT- 0, I, II and III complexes.[3; 7-9] In the final stage of this process, ILVs are released into the MVB lumen by the ESCRT-III complex, comprising a number of charged multivesicular body proteins (CHMPs) that are recruited from monomeric cytosolic pools to form a filamentous structure inside the ILV neck. Complex formation is accompanied by a conformational change in the CHMP proteins that exposes C-terminal motifs that bind to MIT (Microtubule-interacting and trafficking) domains in interacting proteins such as VPS4, promoting their endosomal recruitment.[11-14] VPS4 functions as a hexameric ring which, using energy from ATP-hydrolysis, modifies the ESCRT-III complex filaments by unfolding subunits through its central pore – this subunit removal has been proposed to constrict ESCRT-III filaments and tighten the ILV neck.[1; 4]

ESCRT-III proteins and VPS4 also have roles unrelated to membrane modelling, participating in the dynamic control of mitotic spindle morphology and mitotic spindle checkpoint signalling, as well as in multiple aspects of centrosome biology and primary cilium formation. Cells lacking many different individual ESCRT-III or VPS4 proteins develop aberrant nuclei composed of fragmented or interconnected micronuclei, an increased number of centrosomes, multipolar spindles and abnormal chromosome alignment during metaphase.[15] In addition, VPS4 dynamically localises to centrosomes and regulates centrosome function, position, number and morphology.[15; 16] Related to this, loss of VPS4 or over-expression of a dominant negative ATPase-defective VPS4 mutant has also been linked to reduced primary cilium formation independent of ESCRT-III, via a mechanism proposed to involved disrupted centriolar satellite assembly at the centrosome.[16]

Although mutations in the ESCRT-III proteins CHMP1A, CHMP2B and CHMP4B cause autosomal recessive pontocerebellar hypoplasia (MIM 614961), autosomal dominant amyotrophic lateral sclerosis - frontotemporal dementia (MIM 614696) and autosomal

recessive cataract (MIM 605387) respectively, somewhat surprisingly other ESCRT-III-related proteins have not been linked to genetic disease.[17-19] In this study, we have identified and functionally characterised multiple *de novo* heterozygous missense mutations in *VPS4A* (MIM 609982), which cause a severe neurodevelopmental disorder characterised by severe hypotonia and developmental delay (DD), intellectual disability (ID), structural brain abnormalities including thin corpus callosum and ponto-cerebellar hypoplasia, extrapyramidal neurological dysfunction, congenital cataracts with visual dysfunction, sensorineural deafness and haematological abnormalities, providing evidence of an essential function of this ATPase in multiple cellular and developmental processes in humans.

Materials and Methods

Subjects

Clinical data and DNA specimens were collected, stored and used following procedures in accordance with the ethical standards of the declaration of Helsinki protocols, with signed informed consents from the participating subjects or families. The study was approved by the local Institutional Ethical Committee of the Ospedale Pediatrico Bambino Gesù, Rome (1702_OPBG_2018) and the Cambridge South Research Ethics Committee (13/EE/0325). All probands except proband 5 were analysed in the context of dedicated research projects focused on undiagnosed disorders, while proband 5 was referred for diagnostic genetic testing. Explicit permission was obtained to publish the photographs of the subjects shown in Fig. 1.

Genomic analyses

WES and WGS was performed using DNA samples obtained from leukocytes. A trio-based strategy was used in all cases. WES and WGS data processing, and variant filtering and prioritization by allele frequency, predicted functional impact, and inheritance models were performed as previously reported.[20-22] The *de novo* origin of the *VPS4A* mutations was confirmed by Sanger sequencing (primer sequences available on request).

Protein sequence conservation and mapping of variants to homologous VPS4 protein structures

Sequence conservation of VPS4 proteins was analysed across orthologous and paralogous protein sequences for different model species as previously described.[23] Constrained coding regions model was run for gnomAD 2.1.1 exomes.[24]

There are protein structures homologous to human VPS4A in hexameric or monomeric forms in Protein Data Bank (PDB).[25] Because the hexamer is the functional form of VPS4A, first

we mapped all the *de novo* missense variants to the homologous yeast VPS4, since it is the most similar structure to human available in this oligomeric state. This structure has ADP bound and a cyclic peptide in the central pore (PDB ID 6OO2, cryo-EM with resolution 4.4Å).[26] Then, we compared our observations to the monomeric forms using the homologous human and mouse VPS4B, all X-ray crystal structures. These were in apo forms (human PDB ID 1XWI, with resolution 2.8Å; mouse PDB ID 2ZAM, with resolution 3.5Å) and in ATP or ADP bound forms (mouse PDB ID 2ZAN and 2ZAO, with resolution 2.8Å and 3.2 Å respectively).[27; 28] All structures were visualized and aligned with PyMOL version 2.0 (The PyMOL Molecular Graphics System, Version 2.0 Schrödinger, LLC).

Antibodies

Antibidies used: rabbit polyclonal anti-beta III tubulin (ab18207), rabbit polyclonal anti-CHMP2B (ab33174), mouse monoclonal anti-M6PR (ab2733), mouse monoclonal anti-MAP2 (ab11268), rabbit polyclonal anti-pericentrin (ab4448), rabbit polyclonal anti-Tau (ab64193) from Abcam; mouse monoclonal anti-CD63 (clone H5C6; Developmental Studies Hybridoma Bank, University of Iowa); rabbit polyclonal anti-Cathepsin D (219361), rabbit polyclonal anti-Histone H2A.X (07-627), mouse monoclonal anti-myc (clone 4A6, 05-724) from EMD Millipore; mouse monoclonal anti-TfnR (13-6800), mouse monoclonal Anti-BrdU (B35130) from Invitrogen; IRDye-conjugated secondary antibodies from LICOR; rabbit polyclonal anti IST1 (51002-1-AP) from Proteintech Group; mouse monoclonal anti-SNX1 (611582), anti-EEA1 (610456), anti-Rab5 (610742) from BD transduction laboratories; mouse monoclonal anti-CHMP6 (clone B-3; sc-398963), mouse monoclonal anti-EGFR (clone A-10, sc-373746), mouse monoclonal anti-LAMP1 (H4A3), mouse monoclonal anti-lamin A/C (E-1: sc-376248), mouse monoclonal anti-acetylated α-tubulin (sc-23950), mouse monoclonal VPS4A (clone A-11, sc-393428) from Santa Cruz Biotechnology, Inc; horseradish peroxidase (HRP)-conjugated secondary antibodies, mouse

monoclonal anti-β-tubulin (T4026) from Sigma-Aldrich; rabbit polyclonal anti-GAPDH (2118), mouse monoclonal anti-Nanog (clone 1E6C4, 4893), rabbit polyclonal anti-oct-4 (2750), rabbit polyclonal anti-Sox2 (2748) from Cell Signalling Technology; Alexa Fluor 488-, 594- and 568-labelled secondary antibodies for immunofluorescence from Molecular Probes.

Constructs

Lentiviral plasmids used the A62 backbone and the packaging plasmids pMD VSV-G and pCMV Δ8.91. A62-myc-*VPS4A* was generated by cloning *VPS4A* from pLNCX2-mCherry-*VPS4A* into the A62 vector (NheI-EcoRI) with the addition of an N-terminal myc tag. Mutant versions of A62-myc-*VPS4A* (p.R284G, p.R284W, p.E228Q, p.E206K, p.I337V and p.P168S) were generated by site-directed mutagenesis. sgRNA sequences targeting the transcription start site of *VPS4A* were selected from the Weissman CRISPRi-v2 library.[29] Sense and antisense sgRNA oligonucleotides were designed with 5'CACC and 3'CAAA overhangs, respectively and cloned into pKLV-U6gRNA-EF(BbsI)-PGKpuro2ABFP (BpiI) for lentivirus production. The following sgRNA were used:

Scrambled: GGGACGCGAAAGAAACCAGT

VPS4A G1: GGCAGGGCGGCCGCTCGCAG

VPS4A G2: GACTCGGCTCCCGCTGCGAG

VPS4A G3: GGGAGCCGAGGTACTGGGTC

pLNCX2-mCherry-VPS4A was a gift from Sanford Simon (Addgene plasmid # 115334; RRID:Addgene_115334). pKLV-U6gRNA-EF(BbsI)-PGKpuro2ABFP was a gift from Kosuke Yusa (Addgene plasmid # 50946; RRID:Addgene_50946). A62 was a gift from Michael Fernandopulle (University of Cambridge, UK).

Cell Culture

Proband fibroblasts, HeLaM and HEK-293T cells were grown in complete Dulbecco's Modified Eagle's Medium (DMEM, Sigma-Aldrich) supplemented with 10% foetal bovine serum (FBS, Sigma-Aldrich), 100 U/mL penicillin and 100 µg/mL streptomycin (Sigma-Aldrich) and 2 mM L-Glutamine (Sigma-Aldrich). Human i[3]N and CRISPRi-i[3]N iPSCs (generated in a WTC11 iPSC background line) were a gift from Michael Ward (NIH, Bethesda, USA). iPSCs were cultured in TESR-E8 (STEMCELL Technologies) on dishes coated with Matrigel Matrix (Corning). TESR-E8 was replaced daily and cells were passaged at 80%-90% confluency with 0.5 mM EDTA to maintain colony growth and with the ROCK inhibitor Y-27632 (10 µM, Tocris). CRISPRi-i[3]N iPSCs stably expressing pKLV were additionally cultured in the presence of 2 µg/mL puromycin (Sigma-Aldrich). All cell lines were cultured with 5% CO_2 at 37°C and were regularly tested for mycoplasma contamination.

HeLa Cell transfection

HeLa cells were transfected with purified plasmid using polyethylenimine (PEI, Sigma-Aldrich). In brief, a mixture of 50 µL optiMEM and 1.69 µg of DNA was prepared and incubated at room temperature for 5 minutes. Another mixture containing 150 µL optiMEM and 3.38 µL PEI was prepared and incubated for 5 minutes. Both solutions were then mixed together and incubated for 20 minutes. The total volume was then added to one well of a 6-well plate, already containing 1.5 mL of DMEM supplemented with 10% FBS and 2 mM L-Glutamine. Cells were typically transfected 24 h after plating and incubated with transfection reagents for 29 h.

I[3]Neuron differentiation

Differentiation into i[3]Neurons was as previously described, with slight modifications.[30] Briefly, on Day 0 iPSCs were dissociated into single cells using StemPro Accutase (Thermo Fisher Scientific) and seeded at a density of 150,000 cells/cm^{2} on Matrigel-coated culture

dishes in Induction Medium (IM) composed of DMEM/F-12, 1X N-2 Supplement, 1X MEM

Non-Essential Amino Acids Solution, 1X GlutaMAX Supplement (all Thermo Fisher

Scientific), 10 µM Y-27632 and 2 µg/mL doxycycline hydrochloride (Sigma-Aldrich). Pre-

differentiated cells were maintained in IM for 3 days with daily medium changes. After the 3-

day differentiation period, cells were dissociated with StemPro Accutase and seeded at 5 x

10^4 cells/cm^2 onto culture plates coated with 0.1 mg/mL poly-L-ornithine (Sigma-Aldrich).

Cells were maintained in Cortical Neuron Culture Medium, composed of BrainPhys

Neuronal Medium (STEMCELL Technologies), 1X B-27 Supplement (Thermo Fisher

Scientific), 10 ng/mL BDNF (PeproTech), 10 ng/mL NT-3 (PeproTech) and 1 µg/mL mouse

Laminin (Thermo Fisher Scientific) with half media changes carried out every 3-4 days.

Stable cell lines

Stable cell lines were generated by lentiviral transduction of iPSCs with the VPS4A and

sgRNA lentivectors described earlier. Briefly, HEK-293T cells were co-transfected with a

lentiviral expression construct and the packaging vectors pCMVΔ8.91 and pMD VSV-G at a

ratio of 1:0.7:0.3 using TransIT-293 (Mirus Bio) as per the manufacturer's instructions. The

viral supernatant was collected 48 h post-transfection, passed through a 0.45 µm filter, and

added to target cells in the presence of 10 µg/mL polybrene (Sigma-Aldrich). Typically,

following spinoculation at 1800 rpm for 1h at 32°C, cells were transduced for 16 h.

Transduced cells were selected by adding puromycin at a final concentration of 1 µg/mL

from 24 h if required.

Immunoblotting

Cells were washed twice on ice with PBS and subsequently scraped with ice-cold Triton X-

100 lysis buffer (1% Triton X-100, 150 mM NaCl, 50 mM HEPES pH 7.4, 1 mM EDTA,

10% (v/v) glycerol and protease inhibitors). Samples were centrifuged at 20,000 g for 10

minutes at 4°C. Sample buffer was added to supernatant and samples were heated at 95°C for 5 minutes. Proteins were resolved by SDS-PAGE and transferred to a PVDF membrane. Membranes were blocked in 5% (w/v) skimmed milk powder in PBS containing 0.1% Tween 20 for 30 minutes at room temperature before being probed with primary and secondary antibodies. Membranes were visualised using an ECL Western Blotting Detection Kit (GE Healthcare) for HRP-conjugated antibodies or, for IRDye-conjugated secondary antibodies, imaged directly for infrared fluorescence signal detection on an Odyssey Infrared Imaging System using LICOR Image Studio software (LICOR, US). Western blots were quantified by densitometry using ImageJ.

Analysis of centrosome and mitotic spindle number, morphology and chromosome segregation

After 24 h of culture in complete medium, fibroblasts were treated with 2 mM thymidine (Sigma-Aldrich) for 24 h, washed with PBS 1X, recovered with complete medium for 3 h and then treated with 100 ng/ml nocodazole (Sigma-Aldrich) for 12 h. Afterwards, fresh drug-free medium was added and recovery was allowed for the different time points (15 to 120 minutes) by fixing cells every 15 minutes using PHEMO buffer for 10 min at room temperature.

Primary cilium analysis

Cells were plated onto coverslips, maintained for 24 h in low serum medium to promote emission of cilia and then fixed in absolute chilled methanol for 10 minutes at -20°C.

BrdU assay

Assessment of cells in the different cell cycle phases was performed by dual flow cytometry analysis of cells incorporating BrdU and stained with the fluorescent DNA probe propidium iodide (PI). Briefly, cells were incubated for 1 h with BrdU (Sigma-Aldrich) at a final concentration of 30 μM. Then, BrdU was removed, cells were rinsed with PBS prior

harvesting, and permeabilized using ice-cold 100% ethanol. Cells were incubated with HCl 3N to denature DNA, and 0.1 M sodium tetraborate to stop this reaction. Finally, fibroblasts were incubated with an anti-BrdU antibody followed by goat anti-mouse Alexa Fluor 488 secondary antibody. Cells were then re-suspended in a buffer containing 10 μg/ml RNase A and 20 μg/ml PI and immediately analysed by FACS.

Cytokinesis-block micronucleus and chromosome aberration assays

The cytokinesis-block micronucleus assay was conducted following a previous protocol.[31] In actively dividing cells, cytokinesis was blocked with 4.5 μg/ml cytochalasin B (Sigma-Aldrich), an inhibitor of actin polymerization. Twenty four hours later, cells were collected by cytospin centrifugation (Shandon Cytospin 3, Thermo Fisher Scientific) at 600 r.p.m for 5 min and fixed in absolute methanol at −20°C for 10 min. Slides were stained with 3% Giemsa (Sigma-Aldrich) in Sorensen buffer, pH 6.8, and the analysis was performed by using an optical microscope. Cells were analysed following previously reported criteria.[31]

Chromosome aberrations were analysed in mitotic cells obtained from actively dividing cells treated for 2 hours with colcemid (0.1 μg/ml, Sigma-Aldrich). Cells were harvested by standard procedures. Briefly, after 10 min incubation at 37°C in 0.075 M KCl, fibroblasts were fixed three times with cold methanol/acetic acid (3:1). Slides were prepared by a conventional air-drying technique and stained with 5% Giemsa in Sorensen buffer pH 6.8.

Immunofluorescence microscopy on fixed cells

Cells were fixed at room temperature in 3.7% (v/v) formaldehyde in PBS and permeabilised in PBS containing 0.1% (v/v) saponin (Sigma-Aldrich) or 0.1% (v/v) Triton X-100 (Sigma-Aldrich). Coverslips were labelled with primary and secondary antibodies as previously described.[32] Slides were analysed with a LSM980 confocal microscope (63x NA 1.40 oil immersion objective, 37°C), LSM880 confocal microscope (100x or 63x NA 1.40 oil

immersion objective, 37°C), LSM780 confocal microscope (63x NA 1.40 oil immersion objective, 37°C), Leica TCS SP2 AOBS confocal microscope (63x NA 1.40 oil immersion objective, 37°C) or an AxioImager Z2 Motorized Upright Microscope (100x or 63x NA 1.40 oil immersion objective, room temperature, Axiocam 506; ZEISS). Images were subsequently processed using Huygens Professional software for deconvolution, ImageJ, Adobe Photoshop and Adobe Illustrator.

Image analysis and quantitation

To determine the percentage of cells with large marker-positive endosomes, the largest organelle per cell was measured using ImageJ, with at least 100 cells recorded per experimental condition. For quantification of the mean number of puncta per cell, images of ≥20 cells per condition were analysed using the ImageJ 'analyse particles' command. Co-localisation analysis was performed by a) individual puncta were first delineated by intensity thresholding in ImageJ and the number of co-localised puncta were then counted manually for 5 cells (proband fibroblasts) or ≥ 20 cells per condition per experimental replicate (i[3]Neurons), or b), the extent of co-localisation was determined by calculating the Pearson's correlation coefficient for red and green pixels in each cell using the Coloc2 ImageJ plugin for 10 cells per condition. To assess the percentage of cells with aberrant centrosome number, ≥25 cells were analysed in each of the 6 biological repeats for each experimental condition (200 cells/line). To assess the percentage of cells with aberrantly shaped nucleus, ≥40 cells were analysed in each of the 4 biological repeats for each experimental condition (200 cells/line). To assess the percentage of cells with micronuclei and nucleoplasmic bridges, 200 cells (micronuclei) or 250 (nucleoplasmic bridges) were analysed in each of the 5 (micronuclei) or 4 (nucleoplasmic bridges) biological repeats for each experimental condition (1000 cells/line). For the analysis of chromosome aberrations, ≥30 well-spread metaphases were analysed in each of the 3 biological repeats for each experimental condition (100

cells/line). Since fixation procedures may often result chromosome loss, the analysis was restricted to metaphases containing 45-46 chromosomes. To assess DNA damage, ≥40 cells were analysed in each of the 4 biological repeats for each experimental condition (200 cells/line), counting only cells showing more than 20 foci positive to γ-H2AX staining. Finally, for determining the amount of cells with aberrant primary cilium, a total of 100 cells were analysed for each cell line over two experiments.

Statistical analysis

Statistical analysis and *post hoc* tests were carried out as described in figure legends using GraphPad Prism 8. The statistical significance is denoted on graphs by asterisks (*), where *$P<0.05$, **$P<0.01$, ***$P<0.001$ and n.s = not significant.

Results

Genetic Analysis

Using data from GeneMatcher, the UK National Institute for Health Research Bioresource and Genomics England Research Consortium,[33] or repositories linked to diagnostic testing (GeneDx Laboratory), 6 unrelated individuals with *de novo* variants in *VPS4A* (NM_013245.3) were identified. All had a common and distinctive phenotype including microcephaly, profound neonatal onset of hypotonia and global developmental delay, with similar structural brain abnormalities and cataracts in the majority.

Five of the probands had *de novo* heterozygous missense variants at amino acid position 284. These included four (Probands 1, 3, 4 and 5) who had a c.850A>T (p.Arg284Trp) substitution and a single case (Proband 2) with a c.850A>G (p.Arg284Gly) change. Three of these cases were identified from a trio-based whole genome sequencing (WGS) approach (Probands 1, 3 and 4),[34; 35] whilst the others were identified using trio-based whole exome sequencing (WES) in the context of the Undiagnosed Patients Program at the Ospedale Pediatrico Bambino Gesù (Proband 2) or within routine care by GeneDx Laboratory (Proband 5). In addition, trio WGS in a further case identified a *de novo* variant at c.616G>A (p.Glu206Lys; Proband 6). In each case, there was a single plausible *de novo* variant in the absence of any pathogenic variant in genes previously associated with Mendelian diseases. Subsequent WGS in Proband 2 further excluded the occurrence of other clinically relevant variants. The DNA variants causing the p.Arg284 and p.Glu206 alterations were not present in control population databases (gnomAD, ExAC, TOPMed), fell in regions highly constrained for variation in control populations (Fig. 1A) and affected conserved amino acids of the AAA ATPase domain of VPS4A that are invariable across VPS4 family members from multiple species (Fig. S1). They had strong computational evidence for pathogenicity (Table S1).

Two DNA variants c.502C>T (p.Pro168Ser) and c.1009A>G (p.Ile337Val), were also observed in one and three unrelated families respectively from the Genomics England Research Consortium. These were also absent from gnomAD. However, the mode of inheritance of the variants was unavailable and the pathogenicity of these substitutions was less plausible computationally, with lower CADD (25 and 23) and REVEL scores (0.911 and 0.336) respectively. Additionally, the clinical phenotype of the probands was of non-specific ID, without the distinctive features that were prominent in the other subjects, so these variants were assessed as having uncertain significance.

Mapping of putative pathogenic missense variants in VPS4A to homologous VPS4 protein structure

Protein structural mapping of the putative pathogenic variants to the yeast VPS4 homologous protein structure revealed their proximity to the ATP catalytic site and the pore lining loops. Arg284 was a hot-spot of *de novo* mutations in our subjects. It is one of two arginine residues known as the arginine fingers, a motif that is part of the interface between chains of the hexamerised VPS4, where the catalytic active site is assembled (Fig. 1B-D). Mutations of equivalent arginine finger residues have been studied in multiple ATPases, and cause complete loss of *in vitro* or *in vivo* catalytic activity of the protein, indicating that they are necessary for ATP hydrolysis.[36] The arginine fingers may also be important for oligomerisation of ATPase protein complexes.[36] Thus, existing functional data strongly support a deleterious effect of mutations affecting Arg284.

In contrast, the Glu206 residue is functionally uncharacterised. It is located by the N-terminal of the α3-helix in the boundary with the Pore loop 1 (Fig. 1B-D). The lateral chain of Glu206 (Glu211 in yeast) points to the α5-helix that is on top and connected to Pore loop 2 in all the chains of the hexamer (Fig. 1B-D, Fig. S2A). Pore loops 1 and 2 are very flexible and shape the central pore of the hexamer in ATPases. In the yeast structure both interact with a

synthetic peptide that mimics ESCRT-III proteins, highlighting their role on the translocation of these proteins through the pore (Fig. 1D).[26] The replacement of Glu206 by lysine introduces a change from a negative to a positively charged and slightly bigger lateral chain. Additionally, mapping of this position to the monomeric human and mouse VPS4B shows that the Glu213 (equivalent to Glu206) adopts different orientations, and the N-terminal of the α3-helix is slightly unfolded with the coordinates of Pore loop 1 unresolved (Fig. S2B), suggesting a possible conformational change in this region between the monomeric and hexameric forms. Therefore, we suggest that this variant is likely to affect the fold of the N-terminal of α3-helix, the flexibility of the Pore 1 loop and the lateral interactions between α3 and α5 helices, hence resulting in alterations in the recognition and translocation of ESCRT-III proteins.

Clinical profile of probands

The six probands with *de novo* substitutions affecting Glu206 and Arg284 had a consistent phenotype characterized by severe DD, profound ID and dystonia (Figs. 1E, S3, Table S1, see Supplemental Note). Children were very delayed in establishing head control and none achieved independent walking. Other common findings were cerebellar hypoplasia (five individuals out of six, the other showing uncharacterized severe cerebral atrophy) with a variable degree of corpus callosum hypoplasia. One individual also had bilateral polymicrogyria. Epilepsy was present in three and dystonia in five. Eye involvement was also a common finding, including congenital cataract, retinal dystrophy, and in one case congenital Leber amaurosis. Four individuals were diagnosed with hepatosplenomegaly and/or steatosis. Three subjects had anaemia, which was characterised as dyserythropoietic in two. Severe feeding difficulties were present in four individuals, requiring assisted feeding in three. Two had sensorineural deafness. Severe growth retardation, generally for all parameters, was present in most cases. Notably, severe microcephaly (typically with Z scores < -5) was

universal. Overall, the disorder seems to have a poor prognosis as two affected individuals died in childhood or early adult life (Table S1).

In general, the affected individuals presented with a complex and severe phenotype with some features reminiscent of a ciliopathy-related disorder (cerebellar hypoplasia, retinal dystrophy or Leber amaurosis, sensorineural deafness), a significant neurodevelopmental condition (severe microcephaly and ID), and other features including cataracts, hepatosplenomegaly and congenital anaemia, giving rise to a distinct syndrome.

VPS4A disease-associated variants have a dominant negative effect on endosomal morphology

To investigate the molecular pathological mechanism of the disease-associated VPS4A alterations, we first examined the cellular expression of VPS4A, and found no alteration in protein abundance in fibroblasts from individuals with *de novo* p.Arg284Trp or p.Arg284Gly substitutions versus healthy parental controls, suggesting that mutant protein stability is unaltered (Fig. 2A,B).

The published, rationally designed VPS4A-Glu228Gln mutant and the equivalent VPS4B mutant (p.Glu235Gln) are ATP hydrolysis-defective. Cultured cells over-expressing either of these mutants develop significantly enlarged endosomal vacuoles, caused by a dominant negative effect of incorporation of the ATPase-defective protein into VPS4 hexamers and subsequent failure of disassembly of the ESCRT complexes, which in turn makes ESCRT proteins unavailable for subsequent rounds of ILV formation.[37-39]

 We used this phenotype to interrogate whether the identified disease-associated variants have a dominant negative effect on VPS4A function. We first confirmed that, as expected, expression of VPS4A-Glu228Gln in HeLa cells caused an enlarged endosomal vacuolar phenotype, in contrast to wild-type VPS4A, which exhibited a pan-cytosolic distribution

consistent with its known expression pattern (Fig. 2C, D). Expression of VPS4A-Arg284Trp, VPS4A-Arg284Gly or VPS4A-Glu206Lys caused the development of vacuolar endosomal structures identical to those generated by VPS4A-Glu228Gln expression (Fig. 2E-G). In contrast, the expression pattern of VPS4A-Pro168Ser and VPS4A-Ile337Val resembled that of wild-type VPS4A (Fig. 2H, I). We concluded that the p.Arg284Trp, p.Arg284Gly and p.Glu206Lys amino acid substitutions exert a dominant negative effect on VPS4 hexamer function, while the p.Pro168Ser and p.Ile337Val sequence changes do not; considered with the clinical and bioinformatics data above, this suggests that the latter two variants are unlikely to be pathogenic.

Physiological expression of disease-associated VPS4A causes abnormal endolysosomal morphology in proband fibroblasts

We examined whether physiological expression of heterozygous p.Arg284Trp or p.Arg284Gly mutants in proband-derived fibroblasts caused altered endosomal morphology. We did not observe extremely large vacuolar structures of the type observed in cells over-expressing exogenous ATPase-defective VPS4. However, the proband-derived cell lines had an increase in the percentage of cells with larger vesicles labelled by EEA1 (an early endosome marker), CD63 (which is typically enriched in the ILVs of the late endosome) and LAMP1 (enriched in lysosomes), in the absence of significant alterations in the total number of endosomal structures of each compartment (Fig. 2J-L). We did not observe any increased co-localisation between early endosomal, late endosomal or lysosomal markers in proband cells (Fig. S4). Thus heterozygous expression of mutant VPS4A at endogenous levels causes significant enlargement of multiple endosomal compartments, without apparent content mixing between them.

Localisation and known functions of the core ESCRT-III complex at endosomes are not defective in proband fibroblasts

As cells over-expressing dominant negative ATPase-defective VPS4 develop accumulations of ESCRT proteins on enlarged endosomal structures, we investigated whether the proband fibroblasts showed similar aberrant endosomal ESCRT-III localisation. We examined the ESCRT-III protein CHMP2B, a core ESCRT-III component that is recruited to the endosomal membrane during ILV formation. Surprisingly, there was no alteration in the number of cellular CHMP2B puncta with an area greater than $0.1 \ \mu m^2$, or in the percentage of EEA1- or CD63-positive endosomes that were associated with CHMP2B puncta (Fig. S5A,B).

We examined late endosomal ultrastructure in the proband cell lines. Consistent with the light microscopy findings, large endosomes appeared to be more prominent. However, endosomes were still competent to make ILVs, a key function of ESCRT-III, as ILVs within MVBs were readily observed in the proband cells (Fig. S5C).

Efficient degradation of the epidermal growth factor receptor (EGFR) involves sorting to the ILVs of the MVB, via a mechanism that requires core ESCRT-III components.[40] EGFR degradation is inhibited by VPS4B depletion, either alone or combined with VPS4A depletion, or by expression of dominant negative ATPase-defective VPS4B-Glu235Gln.[38; 41-43] To our knowledge the specific role of VPS4A in this process has not been investigated. We examined EGFR degradation in proband fibroblasts carrying the VPS4A-Arg284Trp or VPS4A-Arg284Gly mutants and, consistent with the retained competence of these cells to make ILVs and regulate endosomal localisation of core ESCRT-III components, we found that it was not inhibited; indeed EGFR degradation was increased at 180 minutes post internalisation (Fig. S5D).

We concluded that heterozygous expression of mutant VPS4A in proband cells does not affect the cellular distribution of a core ESCRT-III complex member, prevent formation of ILVs, or adversely affect the degradation of EGFR.

The atypical ESCRT-III protein IST1 accumulates on endosomes in proband fibroblasts

ESCRT-III proteins also play a role in fission of endosomal sorting tubules from the parent endosome. Rather than involving the core ESCRT-III complex, this activity is mediated by a complex formed of two atypical ESCRT-III proteins, IST1 and CHMP1B.[5; 6; 44] Suitable antibodies are available to visualise IST1 by immunofluorescence. At steady state IST1 is localised in juxtaposition with early endosomal markers, and it is recruited to endosomal membranes by dominant negative VPS4A-Glu228Gln.[45] We examined the appearance and localisation of IST1 and observed an increased number of IST1 puncta and increased percentage of EEA1-positive endosomes associated with IST1 puncta in proband-derived fibroblasts with the p.Arg284Trp or p.Arg284Gly substitutions, consistent with the idea that VPS4A ATPase activity is required to regulate the association of IST1 with endosomes (Fig. 3A). No increased recruitment of IST1 to late endosomes or lysosomes was observed (Fig. S6). HeLa cells lacking IST1 show increased tubulation of the endosomal tubular marker SNX1 caused by a failure of endosomal tubule fission,[6] but we did not consistently observe this phenotype in the proband fibroblasts (Fig. 3B).

We concluded that heterozygous *VPS4A* mutations cause aberrant accumulations of the atypical ESCRT-III protein IST1 on endosomal membranes.

Human neurons lacking VPS4A exhibit similar endosomal phenotypes to proband fibroblasts

In view of the prominent neurodevelopmental phenotype observed in probands affected by VPS4A mutants, we attempted to model their effect in human neurons. We first generated i[3] iPSC lines expressing the VPS4A-Arg284Trp or -Arg284Gly mutants, using lentiviral transduction of appropriate constructs. In contrast to lines expressing wild-type VPS4A, these lines showed no detectable exogenous VPS4A expression by immunoblotting, and only very

sparse expression (<1% of cells) was observed by immunofluorescence. Those cells that did express the mutant VPS4A exhibited enlarged, vacuolar endosomal structures typical of dominant negative VPS4 mutants (Fig. S7).[37-39] In i[3] iPSCs, the neurogenic transcription factor NGN2 is integrated under a doxycycline-responsive promoter at a safe harbour locus in the WTC11 iPSC line.[46] This experimental system allows simple and rapid generation of glutamatergic cortical neurons (i[3]Ns) upon brief culture of the iPSCs in the presence of doxycycline; the cells have morphological and biochemical properties of neurons 14 days post-induction, and are electrically active after 21 days (Fig. S8).[46] However, no VPS4A-mutant expressing cells were identified upon differentiation of the i[3] iPSCs to neurons and we concluded that over-expression of these altered proteins is incompatible with neuronal survival.

In light of the apparent dominant negative effect of the over-expressed VPS4A mutants, we reasoned that lack of VPS4A may have similar cellular consequences to heterozygous physiological expression of VPS4A mutants that are capable of blocking the function of the wild-type protein, and so may provide useful insights into the potential functional effects of the mutants in neurons. In addition, analysis of neurons lacking VPS4A will elucidate the physiological role of VPS4A in these cells. We therefore employed a modified i[3] iPSC system, in which CRISPR-inhibition (CRISPRi) machinery is integrated into a safe harbour locus.[47] In CRISPRi, an enzymatically dead Cas9 fused to a KRAB transcriptional repressor is targeted close to the transcriptional start site of a target gene by a single guide RNA (sgRNA), thereby inhibiting expression of the gene. This system has advantages over standard CRISPR-based knock-out systems, including high specificity with strikingly few off-target effects and low toxicity.[48] We targeted *VPS4A* for repression in CRISPRi-i[3] iPSCs, using two independent sgRNAs, confirmed cellular depletion of VPS4A in the iPSCs, then differentiated each line to i[3]Ns (Fig. 4A, B). We examined endosomal morphology in these neurons at 14

days differentiation. While there was no significant increase in the percentage of neurons that had enlarged EEA1-positive puncta (Fig. 4C), we observed a significant increase in the percentage of cells with enlarged structures marked by CD63, LAMP1 or the lysosomal enzyme cathepsin D (Fig. 4D, E). In addition, there was an increase in the number of IST1 puncta per cell and of IST1 localisation on early and late endosomal structures (Fig. 5A, B). No difference in the number of puncta of the core ESCRT-III component CHMP6 was observed (Fig. 5C).

We concluded that VPS4A regulates endosomal size and endosomal membrane localisation of the atypical ESCRT-III protein in human neurons, and that loss of VPS4A in neurons largely recapitulates phenotypes that are observed in proband cells expressing dominant negative VPS4A at physiological heterozygous levels.

VPS4A mutants affect centrosome and mitotic spindle organization, and are associated with aberrant chromosomal segregation and G2/M cell cycle arrest

Centrosomes serve as solid-state signaling platforms to dynamically regulate a wide array of cellular structures and processes. The ESCRT-III complex and VPS4 proteins are required to maintain normal centrosome morphology and function, and their silencing alters centrosome and spindle pole numbers, frequently producing multipolar spindles and defects in chromosome segregation and nuclear morphology.[15] To further validate the functional relevance of the identified *VSP4A* mutations we analysed centrosome and mitotic spindle organization in synchronized proband-derived fibroblasts carrying the heterozygous p.Arg284Trp or p.Arg284Gly substitutions. As expected, in interphase, control cells typically had two discernible centrosomes (Fig. 6A). Similarly, during mitosis, these cells formed normal bipolar spindles with two centrosomes. In metaphase, canonical mitotic spindles with properly aligned chromosomes were observed in the vast majority of cases (Fig. 6B). In contrast, proband fibroblasts showed an anomalous centrosome number and morphology in

interphase (Fig. 6A); similarly, multipolar spindles were observed during mitosis, resulting in a high frequency of aberrant chromosome alignment during metaphase (Fig. 6B). Aberrant chromosome segregation was documented by the presence of both lagging and bridging chromosomes during anaphase and telophase (Fig. 6B), and was associated with polyploidy and production of micronuclei, i.e. encapsulated lagging chromosomes or damaged chromosome fragments not incorporated in the main nucleus after anaphase (Fig. 7A). Consistent with these findings, a high proportion of proband fibroblasts were observed at G2/M, as measured by BrdU incorporation flow cytometry analysis (Fig. 7B), which possibly results from altered G2/M and abscission checkpoint activation and/or a faulty progression towards cell division.[49-51]

Proband fibroblasts have abnormal nuclear envelope morphology and increased DNA damage

During anaphase, when chromosome separation has been achieved, the nuclear envelope is reassembled around the forming nuclei, to coordinate proper segregation of the nuclear content in daughter cells and assure the structural integrity and functionality of the nuclear compartment. The ESCRT-III complex and VPS4A and B contribute to nuclear envelope sealing and spindle disassembly at the nuclear envelope-microtubule intersection sites during mitotic exit,[52; 53] and defective ESCRT function causes abnormal nuclear membrane sealing and altered morphology.[54; 55] Moreover, the ESCRT-III complex contributes to repair of nuclear envelope ruptures during interphase, and expression of a dominant negative VPS4A protein delayed repair.[56; 57] Based on these considerations, we explored possible changes in nuclear morphology and architecture in proband fibroblasts expressing the VPS4A-Arg284Trp or -Arg284Gly mutants. Immunofluorescence microscopy with the nuclear envelope marker lamin A/C labelling demonstrated a significant increase in the proportion of proband-derived cells with irregular nuclear morphology compared to control cells (Fig. 8A).

It has been established that nuclear deformation may result in a breaking of the nuclear envelope, which in turn exposes chromosomal DNA to the cytoplasmic environment, thus promoting DNA damage. Consistent with this, immunofluorescence microscopic identification of γH2AX foci, a marker of damaged DNA, showed an increased number of positive cells and foci per cell among those carrying the VSP4A mutants compared to control cells (Fig. 8B), indicating increased spontaneous DNA damage. Thus nuclear envelope morphology and integrity are altered in fibroblasts from individuals with heterozygous VPS4A mutations.

Defective VPS4A function affects primary cilium morphology

Vesicular trafficking plays an essential role in cilium biogenesis and function. Of note, VPS4 has been identified as a dynamic component of the ciliary transition zone, a region in which the mother centriole, tethering to plasma membrane by the transition fibres, becomes the basal body for primary cilium formation. Defective VPS4A ATP hydrolysis causes a block of ciliogenesis after formation of the ciliary vesicle and this function appears to be ESCRT-III-independent.[16] We therefore analysed primary cilium biogenesis and morphology in fibroblasts from affected subjects. Assessment of cilium structure in starved fibroblasts revealed the presence of aberrant primary cilium formation in both fibroblast lines with mutated VPS4A alleles. Specifically, normal cilia were absent in fibroblasts expressing the VPS4A-Arg284Gly mutant, which instead showed a visible basal body (dot cilium); similarly, a dot cilium was documented in most fibroblasts heterozygous for the p.Arg284Trp substitution, although a small number of elongated cilia were also observed in cells from this proband (Fig. 8C). Thus defective VPS4A has pleiotropic consequences on diverse cellular processes, including perturbation of a variety of centrosome-dependent structures.

Discussion

The ESCRT-III complex and VPS4 together form a multifunctional membrane modelling machinery. Against the background of the multiplicity of functions ascribed to ESCRT-III, it is perhaps surprising that only three complex members, CHMP1A, CHMP2B and CHMP4B, have been implicated in Mendelian genetic disease thus far.[17-19] This may be explained by functional redundancy between ESCRT-III complex components, or because loss of components might lead to an embryonic lethal phenotype, as has been observed in some, but not all, mouse models lacking specific CHMP proteins.[58; 59] However, we now report a distinct syndromic neurodevelopmental disorder caused by dominantly acting amino acid substitutions in VPS4A, a key enzyme that regulates ESCRT-III function. We propose the acronym CIMDAG (Cerebellar hypoplasia and Cataracts, Intellectual disability, congenital Microcephaly, Dystonia and Dyserythropoeitic Anemia, Growth retardation) to highlight the main clinical features of this syndrome, which may also include other structural brain abnormalities, retinal dystrophy, hepatosplenomegaly and sensorineural deafness. The haematological features of this condition are thoroughly characterised in the accompanying paper.[60]

The pleotropic clinical effects observed in CIMDAG likely reflect the multitude of cellular functions in which ESCRT-III and VPS4A participate, including those demonstrated to be affected by our studies. In the future it will be important to unravel which ESCRT-III and VPS4A functions underlie the pathology of the different clinical phenotypes we observed. The centrosomal and mitotic defects we observed are strong candidates to underlie microcephaly and other growth impairments in CIMDAG. These processes play a crucial role during brain development, including in neurogenesis, neuronal migration and polarity, and defects in them commonly underlie neurodevelopmental diseases.[61] Defects in mitosis have also been linked to dyserythropoietic anaemia and are a feature of the anaemia seen in

CIMDAG.[60; 62] In contrast, congenital cataract is a recognised feature of lysosomal storage diseases and so it may be related to the endolysosomal dysfunction that we observed, which may also be relevant for the health of mature post-mitotic neurons, as it has been implicated in several forms of neurodegeneration.[63] Finally, it is striking that many of the clinical features found in our probands (including cerebellar hypoplasia, retinal dystrophy, Leber amaurosis, DD, ID, cataract, sensorineural deafness and hypogonadism) occur in ciliopathies, and our data support the proposed role of VPS4A in controlling primary cilium morphogenesis.[16; 64] Thus it is possible that abnormal primary cilium function contributes to the CIMDAG phenotype.

Multiple heterozygous *VPS4A* loss-of-function mutations are present in general population databases, indicating that a haploinsufficiency mechanism is unlikely to cause the type of severe early childhood condition that we describe.[65] In contrast, our data and published evidence point to the p.Glu206Lys, p.Arg284Trp and p.Arg284Gly mutants having a dominant negative effect. Over-expression of each of these mutants in immortalised cells caused development of the highly characteristic enlarged endosomal structures that are induced by expression of known dominant-negative forms of VPS4A. Similar, although less marked, enlarged endosomal phenotypes were also observed in proband cells. As VPS4A protein expression was not altered in proband cells, assuming equal expression of wild-type and mutant VPS4A we expect that a large majority of VPS4A hexamers will have impaired function as they will contain at least one mutant subunit. This may explain the similar endosomal phenotypes we observed in proband fibroblasts and iPSC-derived neurons lacking VPS4A.

The archetypal function for VPS4 proteins is in endosomal sorting and our observations elucidate details of the physiological role of VPS4A in this process. Over-expression of dominant negative VPS4A in cultured cells affects ILV formation, causes trapping of ESCRT

proteins on the endosomal membrane and inhibits EGFR degradation.[38; 39] However, a surprising observation in our study was that proband fibroblasts expressing dominant negative *VPS4A* mutations at heterozygous physiological levels showed no obvious effect on ILV formation or EGFR degradation. Consistent with this, we did not observe accumulation of the "core" ESCRT-III complex member CHMP2B on the endosomal membrane, suggesting that functional VPS4A is not required for removal of the core ESCRT-III complex from the endosomal membrane. This may be because of redundancy between VPS4A and VPS4B – previous studies have shown that double knock-down of these proteins is required for formation of a "VPS4-dominant-negative"- type endosomal compartment. An ESCRT-independent ILV formation pathway has also been described, which could also provide an explanation for retained ILV formation.[66; 67] In contrast, the endosomal localisation of IST1 was increased in both proband fibroblasts and iPSC-derived neurons lacking VPS4A, so it appears that VPS4A is absolutely required for recycling of this protein, the best-characterised function of which is in promoting endosomal tubule fission.[5; 6] Further studies will be required to elucidate the functional consequences of this accumulation on endosomal tubule fission dynamics and endosomal receptor traffic, and its relationship to pathogenesis in our probands, but we speculate that the enhanced EGFR degradation we observed in patient fibroblasts may be explained by defective tubular sorting of this receptor away from endosomal degradation.

In summary, we have identified *de novo* missense mutations affecting the key ESCRT-regulation enzyme VPS4A in probands with a distinct multisystem neurodevelopmental condition. Study of the functional effects of the mutations demonstrated that they act by a dominant negative mechanism to cause effects on multiple ESCRT-dependent cellular pathways, and indicate an absolute requirement for proper VPS4A function in neurodevelopment and other physiological developmental processes in humans.

Supplemental Data includes supplemental clinical reports, author list for genomics England research consortium, supplemental methods, eight figures and one table.

Declaration of Interests

The authors declare no competing interests.

Acknowledgements

Web Resources

Online Mendelian Inheritance in Man (OMIM): http://www.omim.org

GnomAD, http://gnomad.broadinstitute.org/

ExAC database, http://exac.broadinstitute.org/

NHLBI Trans-Omics for Precision Medicine (TOPMed), https://www.nhlbiwgs.org/

dbNSFP, https://sites.google.com/site/jpopgen/dbNSFP

ClinVar, https://www.ncbi.nlm.nih.gov/clinvar/

Pfam, https://pfam.xfam.org/

UniProtKB, https://www.uniprot.org/

Protein Data Bank (PDB), https://www.rcsb.org/

Addgene, http://www.addgene.org/

Data and Code Availability

The pathogenic variants identified in this work have been submitted to ClinVar (submission
ID: SUB7923752). WES and WGS datasets have not been deposited in a public repository
due to privacy and ethical restrictions but are available from the corresponding authors on
request. The 100,000 Genomes Project data used in this work are available from the
Genomics England Research Environment, with restrictions to ensure the confidentiality and
appropriate use of the data.

References

1. McCullough, J., Frost, A., and Sundquist, W.I. (2018). Structures, Functions, and Dynamics of ESCRT-III/Vps4 Membrane Remodeling and Fission Complexes. Annual review of cell and developmental biology 34, 85-109.

2. Schöneberg, J., Lee, I.-H., Iwasa, J.H., and Hurley, J.H. (2017). Reverse-topology membrane scission by the ESCRT proteins. Nature reviews Molecular cell biology 18, 5-17.

3. Vietri, M., Radulovic, M., and Stenmark, H. (2020). The many functions of ESCRTs. Nature reviews Molecular cell biology 21, 25-42.

4. Caillat, C., Maity, S., Miguet, N., Roos, W.H., and Weissenhorn, W. (2019). The role of VPS4 in ESCRT-III polymer remodeling. Biochemical Society transactions 47, 441-448.

5. McCullough, J., Clippinger, A.K., Talledge, N., Skowyra, M.L., Saunders, M.G., Naismith, T.V., Colf, L.A., Afonine, P., Arthur, C., Sundquist, W.I., et al. (2015). Structure and membrane remodeling activity of ESCRT-III helical polymers. Science 350, 1548-1551.

6. Allison, R., Lumb, J.H., Fassier, C., Connell, J.W., Ten Martin, D., Seaman, M.N., Hazan, J., and Reid, E. (2013). An ESCRT-spastin interaction promotes fission of recycling tubules from the endosome. J Cell Biol 202, 527-543.

7. Katzmann, D.J., Babst, M., and Emr, S.D. (2001). Ubiquitin-dependent sorting into the multivesicular body pathway requires the function of a conserved endosomal protein sorting complex, ESCRT-I. Cell 106, 145-155.

8. Babst, M., Katzmann, D.J., Snyder, W.B., Wendland, B., and Emr, S.D. (2002). Endosome-associated complex, ESCRT-II, recruits transport machinery for protein sorting at the multivesicular body. Dev Cell 3, 283-289.

9. Babst, M., Katzmann, D.J., Estepa-Sabal, E.J., Meerloo, T., and Emr, S.D. (2002). Escrt-III: an endosome-associated heterooligomeric protein complex required for mvb sorting. Dev Cell 3, 271-282.

10. Maxfield, F.R., and McGraw, T.E. (2004). Endocytic recycling. Nat Rev Mol Cell Biol 5, 121-132.

11. Yang, D., Rismanchi, N., Renvoise, B., Lippincott-Schwartz, J., Blackstone, C., and Hurley, J.H. (2008). Structural basis for midbody targeting of spastin by the ESCRT-III protein CHMP1B. Nat Struct Mol Biol.

12. Stuchell-Brereton, M.D., Skalicky, J.J., Kieffer, C., Karren, M.A., Ghaffarian, S., and Sundquist, W.I. (2007). ESCRT-III recognition by VPS4 ATPases. Nature 449, 740-744.

13. Obita, T., Saksena, S., Ghazi-Tabatabai, S., Gill, D.J., Perisic, O., Emr, S.D., and Williams, R.L. (2007). Structural basis for selective recognition of ESCRT-III by the AAA ATPase Vps4. Nature 449, 735-739.

14. Bajorek, M., Schubert, H.L., McCullough, J., Langelier, C., Eckert, D.M., Stubblefield, W.M., Uter, N.T., Myszka, D.G., Hill, C.P., and Sundquist, W.I. (2009). Structural basis for ESCRT-III protein autoinhibition. Nature structural & molecular biology 16, 754-762.

15. Morita, E., Colf, L.A., Karren, M.A., Sandrin, V., Rodesch, C.K., and Sundquist, W.I. (2010). Human ESCRT-III and VPS4 proteins are required for centrosome and spindle maintenance. Proceedings of the National Academy of Sciences 107, 12889.

16. Ott, C., Nachmias, D., Adar, S., Jarnik, M., Sherman, S., Birnbaum, R.Y., Lippincott-Schwartz, J., and Elia, N. (2018). VPS4 is a dynamic component of the centrosome that regulates centrosome localization of γ-tubulin, centriolar satellite stability and ciliogenesis. Scientific Reports 8, 3353.

17. Skibinski, G., Parkinson, N.J., Brown, J.M., Chakrabarti, L., Lloyd, S.L., Hummerich, H., Nielsen, J.E., Hodges, J.R., Spillantini, M.G., Thusgaard, T., et al. (2005). Mutations in the endosomal ESCRTIII-complex subunit CHMP2B in frontotemporal dementia. Nature genetics 37, 806-808.

18. Shiels, A., Bennett, T.M., Knopf, H.L.S., Yamada, K., Yoshiura, K.-i., Niikawa, N., Shim, S., and Hanson, P.I. (2007). CHMP4B, a novel gene for autosomal dominant cataracts linked to chromosome 20q. American journal of human genetics 81, 596-606.

19. Mochida, G.H., Ganesh, V.S., de Michelena, M.I., Dias, H., Atabay, K.D., Kathrein, K.L., Huang, H.T., Hill, R.S., Felie, J.M., Rakiec, D., et al. (2012). CHMP1A encodes an essential regulator of BMI1-INK4A in cerebellar development. Nat Genet 44, 1260-1264.

20. Flex, E., Martinelli, S., Van Dijck, A., Ciolfi, A., Cecchetti, S., Coluzzi, E., Pannone, L., Andreoli, C., Radio, F.C., Pizzi, S., et al. (2019). Aberrant Function of the C-Terminal Tail of HIST1H1E Accelerates Cellular Senescence and Causes Premature Aging. Am J Hum Genet 105, 493-508.

21. Bauer, C.K., Calligari, P., Radio, F.C., Caputo, V., Dentici, M.L., Falah, N., High, F., Pantaleoni, F., Barresi, S., Ciolfi, A., et al. (2018). Mutations in KCNK4 that Affect Gating Cause a Recognizable Neurodevelopmental Syndrome. Am J Hum Genet 103, 621-630.

22. Turro, E., Astle, W.J., Megy, K., Gräf, S., Greene, D., Shamardina, O., Allen, H.L., Sanchis-Juan, A., Frontini, M., Thys, C., et al. (2020). Whole-genome sequencing of patients with rare diseases in a national health system. Nature 583, 96-102.

23. Sanchis-Juan, A., Hasenahuer, M.A., Baker, J.A., McTague, A., Barwick, K., Kurian, M.A., Duarte, S.T., BioResource, N., Carss, K.J., Thornton, J., et al. (2020). Structural analysis of pathogenic missense mutations in GABRA2 and identification of a novel de novo variant in the desensitization gate. Molecular Genetics & Genomic Medicine n/a, e1106.

24. Havrilla, J.M., Pedersen, B.S., Layer, R.M., and Quinlan, A.R. (2019). A map of constrained coding regions in the human genome. Nature Genetics 51, 88-95.

25. ww, P.D.B.c. (2018). Protein Data Bank: the single global archive for 3D macromolecular structure data. Nucleic Acids Research 47, D520-D528.

26. Han, H., Fulcher, J.M., Dandey, V.P., Iwasa, J.H., Sundquist, W.I., Kay, M.S., Shen, P.S., and Hill, C.P. (2019). Structure of Vps4 with circular peptides and implications for translocation of two polypeptide chains by AAA+ ATPases. Elife 8.

27. Scott, A., Chung, H.-Y., Gonciarz-Swiatek, M., Hill, G.C., Whitby, F.G., Gaspar, J., Holton, J.M., Viswanathan, R., Ghaffarian, S., Hill, C.P., et al. (2005). Structural and mechanistic studies of VPS4 proteins. The EMBO Journal 24, 3658-3669.

28. Inoue, M., Kamikubo, H., Kataoka, M., Kato, R., Yoshimori, T., Wakatsuki, S., and Kawasaki, M. (2008). Nucleotide-dependent conformational changes and assembly of the AAA ATPase SKD1/VPS4B. Traffic 9, 2180-2189.

29. Horlbeck, M.A., Gilbert, L.A., Villalta, J.E., Adamson, B., Pak, R.A., Chen, Y., Fields, A.P., Park, C.Y., Corn, J.E., Kampmann, M., et al. (2016). Compact and highly active next-generation libraries for CRISPR-mediated gene repression and activation. Elife 5.

30. Fernandopulle, M.S., Prestil, R., Grunseich, C., Wang, C., Gan, L., and Ward, M.E. (2018). Transcription Factor-Mediated Differentiation of Human iPSCs into Neurons. Current protocols in cell biology 79, e51.

31. Fenech, M. (2007). Cytokinesis-block micronucleus cytome assay. Nat Protoc 2, 1084-1104.

32. Connell, J.W., Lindon, C., Luzio, J.P., and Reid, E. (2009). Spastin couples microtubule severing to membrane traffic in completion of cytokinesis and secretion. Traffic 10, 42-56.

33. Sobreira, N., Schiettecatte, F., Valle, D., and Hamosh, A. (2015). GeneMatcher: a matching tool for connecting investigators with an interest in the same gene. Hum Mutat 36, 928-930.

34. French, C.E., Delon, I., Dolling, H., Sanchis-Juan, A., Shamardina, O., Mégy, K., Abbs, S., Austin, T., Bowdin, S., Branco, R.G., et al. (2019). Whole genome sequencing reveals

that genetic conditions are frequent in intensively ill children. Intensive care medicine 45, 627-636.

35. Turro E, A.W., Megy K, Gräf S, Greene D, Shamardina O, et al. (2020). Whole-genome sequencing of patients with rare diseases in a national healthcare system Nature 583, 96-102.

36. Wendler, P., Ciniawsky, S., Kock, M., and Kube, S. (2012). Structure and function of the AAA+ nucleotide binding pocket. Biochimica et Biophysica Acta (BBA) - Molecular Cell Research 1823, 2-14.

37. Scheuring, S., Röhricht, R.A., Schöning-Burkhardt, B., Beyer, A., Müller, S., Abts, H.F., and Köhrer, K. (2001). Mammalian Cells Express Two VPS4 Proteins Both of Which are Involved in Intracellular Protein Trafficking. Journal of Molecular Biology 312, 469-480.

38. Fujita, H., Yamanaka, M., Imamura, K., Tanaka, Y., Nara, A., Yoshimori, T., Yokota, S., and Himeno, M. (2003). A dominant negative form of the AAA ATPase SKD1/VPS4 impairs membrane trafficking out of endosomal/lysosomal compartments: class E vps phenotype in mammalian cells. Journal of cell science 116, 401-414.

39. Bishop, N., and Woodman, P. (2000). ATPase-defective Mammalian VPS4 Localizes to Aberrant Endosomes and Impairs Cholesterol Trafficking. Molecular Biology of the Cell 11, 227-239.

40. Bache, K.G., Stuffers, S., Malerod, L., Slagsvold, T., Raiborg, C., Lechardeur, D., Walchli, S., Lukacs, G.L., Brech, A., and Stenmark, H. (2006). The ESCRT-III subunit hVps24 is required for degradation but not silencing of the epidermal growth factor receptor. Mol Biol Cell 17, 2513-2523.

41. Lin, H.H., Li, X., Chen, J.-L., Sun, X., Cooper, F.N., Chen, Y.-R., Zhang, W., Chung, Y., Li, A., Cheng, C.-T., et al. (2012). Identification of an AAA ATPase VPS4B-dependent pathway that modulates epidermal growth factor receptor abundance and signaling during hypoxia. Molecular and cellular biology 32, 1124-1138.

42. Yoshimori, T., Yamagata, F., Yamamoto, A., Mizushima, N., Kabeya, Y., Nara, A., Miwako, I., Ohashi, M., Ohsumi, M., and Ohsumi, Y. (2000). The mouse SKD1, a homologue of yeast Vps4p, is required for normal endosomal trafficking and morphology in mammalian cells. Molecular biology of the cell 11, 747-763.

43. Fraile-Ramos, A., Pelchen-Matthews, A., Risco, C., Rejas, M.T., Emery, V.C., Hassan-Walker, A.F., Esteban, M., and Marsh, M. (2007). The ESCRT machinery is not required for human cytomegalovirus envelopment. Cell Microbiol 9, 2955-2967.

44. Allison, R., Edgar, J.R., Pearson, G., Rizo, T., Newton, T., Günther, S., Berner, F., Hague, J., Connell, J.W., Winkler, J., et al. (2017). Defects in ER–endosome contacts impact lysosome function in hereditary spastic paraplegia. J Cell Biol 216, 1337-1355.

45. Agromayor, M., Carlton, J.G., Phelan, J.P., Matthews, D.R., Carlin, L.M., Ameer-Beg, S., Bowers, K., and Martin-Serrano, J. (2009). Essential role of hIST1 in cytokinesis. Mol Biol Cell 20, 1374-1387.

46. Wang, C., Ward, M.E., Chen, R., Liu, K., Tracy, T.E., Chen, X., Xie, M., Sohn, P.D., Ludwig, C., Meyer-Franke, A., et al. (2017). Scalable Production of iPSC-Derived Human Neurons to Identify Tau-Lowering Compounds by High-Content Screening. Stem Cell Reports 9, 1221-1233.

47. Tian, R., Gachechiladze, M.A., Ludwig, C.H., Laurie, M.T., Hong, J.Y., Nathaniel, D., Prabhu, A.V., Fernandopulle, M.S., Patel, R., Abshari, M., et al. (2019). CRISPR Interference-Based Platform for Multimodal Genetic Screens in Human iPSC-Derived Neurons. Neuron.

48. Kampmann, M. (2018). CRISPRi and CRISPRa Screens in Mammalian Cells for Precision Biology and Medicine. ACS Chem Biol 13, 406-416.

49. Kastan, M.B., and Bartek, J. (2004). Cell-cycle checkpoints and cancer. Nature 432, 316-323.

50. Bartek, J., and Lukas, J. (2007). DNA damage checkpoints: from initiation to recovery or adaptation. Curr Opin Cell Biol 19, 238-245.

51. Caballe, A., Wenzel, D.M., Agromayor, M., Alam, S.L., Skalicky, J.J., Kloc, M., Carlton, J.G., Labrador, L., Sundquist, W.I., and Martin-Serrano, J. (2015). ULK3 regulates cytokinetic abscission by phosphorylating ESCRT-III proteins. Elife 4, e06547.

52. Vietri, M., Schink, K.O., Campsteijn, C., Wegner, C.S., Schultz, S.W., Christ, L., Thoresen, S.B., Brech, A., Raiborg, C., and Stenmark, H. (2015). Spastin and ESCRT-III coordinate mitotic spindle disassembly and nuclear envelope sealing. Nature 522, 231-235.

53. Olmos, Y., Hodgson, L., Mantell, J., Verkade, P., and Carlton, J.G. (2015). ESCRT-III controls nuclear envelope reformation. Nature 522, 236-239.

54. Ventimiglia, L.N., Cuesta-Geijo, M.A., Martinelli, N., Caballe, A., Macheboeuf, P., Miguet, N., Parnham, I.M., Olmos, Y., Carlton, J.G., Weissenhorn, W., et al. (2018). CC2D1B Coordinates ESCRT-III Activity during the Mitotic Reformation of the Nuclear Envelope. Dev Cell 47, 547-563.e546.

55. Asencio, C., Davidson, I.F., Santarella-Mellwig, R., Ly-Hartig, T.B., Mall, M., Wallenfang, M.R., Mattaj, I.W., and Gorjánácz, M. (2012). Coordination of kinase and phosphatase activities by Lem4 enables nuclear envelope reassembly during mitosis. Cell 150, 122-135.

56. Raab, M., Gentili, M., de Belly, H., Thiam, H.R., Vargas, P., Jimenez, A.J., Lautenschlaeger, F., Voituriez, R., Lennon-Duménil, A.M., Manel, N., et al. (2016). ESCRT III repairs nuclear envelope ruptures during cell migration to limit DNA damage and cell death. Science 352, 359-362.

57. Arii, J., Watanabe, M., Maeda, F., Tokai-Nishizumi, N., Chihara, T., Miura, M., Maruzuru, Y., Koyanagi, N., Kato, A., and Kawaguchi, Y. (2018). ESCRT-III mediates

budding across the inner nuclear membrane and regulates its integrity. Nature communications 9, 3379.

58. Shim, J.H., Xiao, C., Hayden, M.S., Lee, K.Y., Trombetta, E.S., Pypaert, M., Nara, A., Yoshimori, T., Wilm, B., Erdjument-Bromage, H., et al. (2006). CHMP5 is essential for late endosome function and down-regulation of receptor signaling during mouse embryogenesis. J Cell Biol 172, 1045-1056.

59. Ghazi-Noori, S., Froud, K.E., Mizielinska, S., Powell, C., Smidak, M., Fernandez de Marco, M., O'Malley, C., Farmer, M., Parkinson, N., Fisher, E.M., et al. (2012). Progressive neuronal inclusion formation and axonal degeneration in CHMP2B mutant transgenic mice. Brain 135, 819-832.

60. Seu, K.G., Trump, L.R., Emberesh, S., Lorsbach, R.B., Johnson, C., Meznarich, J., Underhill, H.R., Chou, S.T., Sakthivel, H., Nassar, N., et al. VPS4A mutations in humans cause syndromic congenital dyserythropoietic anemia due to cytokinesis and trafficking defects. American Journal of Human Genetics in press.

61. Woods, C.G. (2004). Human microcephaly. Curr Opin Neurobiol 14, 112-117.

62. Paw, B.H., Davidson, A.J., Zhou, Y., Li, R., Pratt, S.J., Lee, C., Trede, N.S., Brownlie, A., Donovan, A., Liao, E.C., et al. (2003). Cell-specific mitotic defect and dyserythropoiesis associated with erythroid band 3 deficiency. Nat Genet 34, 59-64.

63. Hu, Y.B., Dammer, E.B., Ren, R.J., and Wang, G. (2015). The endosomal-lysosomal system: from acidification and cargo sorting to neurodegeneration. Translational neurodegeneration 4, 18.

64. Reiter, J.F., and Leroux, M.R. (2017). Genes and molecular pathways underpinning ciliopathies. Nat Rev Mol Cell Biol 18, 533-547.

65. Karczewski, K.J., Francioli, L.C., Tiao, G., Cummings, B.B., Alföldi, J., Wang, Q., Collins, R.L., Laricchia, K.M., Ganna, A., Birnbaum, D.P., et al. (2020). The mutational constraint spectrum quantified from variation in 141,456 humans. Nature 581, 434-443.

66. Theos, A.C., Truschel, S.T., Tenza, D., Hurbain, I., Harper, D.C., Berson, J.F., Thomas, P.C., Raposo, G., and Marks, M.S. (2006). A lumenal domain-dependent pathway for sorting to intralumenal vesicles of multivesicular endosomes involved in organelle morphogenesis. Dev Cell 10, 343-354.

67. Edgar, J.R., Eden, E.R., and Futter, C.E. (2014). Hrs- and CD63-dependent competing mechanisms make different sized endosomal intraluminal vesicles. Traffic 15, 197-211.

Figure Legends

Figure 1. *De novo* missense variants in *VPS4A* mapped to the schematic protein diagram and the homologous yeast structure. A) Allele count of missense variants in gnomAD and the constrained coding regions' (CCRs) percentiles are represented for human VPS4A (NP_037377) and are aligned with protein domains. The *de novo* missense variants cluster in constrained regions of the large ATPase domain. Coordinates of the protein domains were from Pfam (UniProtKB entry Q9UN37). MIT = microtubule interacting and trafficking; AAA = ATPase family associated with various cellular activities; AAA_lid = AAA+ lid domain; Vps4_C = Vps4 C-terminal oligomerization domain; LC = low complexity region. Disordered regions are shaded in translucent grey. **B-D)** *De novo* missense variants in VPS4A are mapped to the cryo-EM structure of the ATPase domain of the homologous yeast VPS4 in homohexameric form (PDB ID: 6OO2). The approximate locations of the active sites are shaded in orange, with the ADP nucleotides represented in sticks, when present. The conserved motifs that define the ATP binding site and pore loops 1 and 2 are shown in dark blue or grey. **B)** Structure of the homohexamer, with the six chains alternately coloured in blue and white. **C)** Structure of a single chain. Both p.R284W and p.R284G are observed to affect the R-finger of the active site and p.E206K affects the intra-chain interface between α3 and α5-helices, located after the pore loops 1 and 2. Only the name of these two helices is shown for clarity. p.E228Q, a rationally-designed mutant that produces dominant-negative ATPase-defective VPS4A, falls in the Walker B motif of the active site. **D)** Zoom in of the inter-chain interface. The pore loops 1 and 2 shape the pore and interact with the synthetic peptide (in yellow) that shows how the ESCRT-III protein would translocate through the pore. **E)** Images of probands at representative ages.

Figure 2. VPS4A disease-associated variants have a dominant negative effect on endosomal morphology. A) Representative VPS4A immunoblots of fibroblast cell lysates

from a proband (Proband 1) with the p.R284W sequence change and her parents (control-1 and control-2), and from a proband (Proband 2) with the p.R284G sequence change. **B)** Immunoblot band intensities from 3 such experiments were quantified, normalised to GAPDH loading control values, and plotted in the corresponding graph. **C-I)** HeLa cells were transfected with constructs expressing wild-type myc-VPS4A, myc-VPS4A containing the rationally-designed ATPase-defective p.E228Q mutant, or myc-VPS4A harbouring the sequence changes identified in probands. Cells were fixed, labelled with anti-Myc and anti-RAB5 antibodies and visualised with confocal microscopy. The inset panels show higher magnification views of the boxed regions- examples of large vacuolar endosomal structures are shown. **J-L)** Cultured fibroblasts from the control subjects and probands indicated were fixed, labelled with EEA1 (early endosomes) (**J**), CD63 (preferentially labels late endosomes) (**K**) and LAMP1 (predominantly labels lysosomes) (**L**), then visualised by widefield immunofluorescence microscopy. The percentage of cells with an endosomal organelle over a nominal cut-off size and the number of labelled organelles per cell was counted in n=3 biological repeats for each marker (in 100 cells per experimental condition in each repeat), then quantified in the corresponding charts. Bars in all plots show mean ± S.E.M., p-values calculated by one-way ANOVA with Tukey's post-hoc test for repeated measures. Scale bars = 10 μm.

Figure 3. The atypical ESCRT-III protein IST1 accumulates on endosomes in proband fibroblasts. A**)** Cultured fibroblasts from control subjects or the probands indicated were fixed, labelled against EEA1 and IST1, then visualised with confocal immunofluorescence microscopy. The number of IST1 puncta per cell and the percentage of EEA1-positive endosomes associated with an IST1 punctum was quantified in 3 such experiments (in 5 cells per experimental condition in each biological repeat) and plotted in the corresponding charts. Arrows indicate juxtaposed or co-localised puncta. **B)** Cultured fibroblasts from control

subjects or the probands indicated were fixed and labelled for the endosomal tubular marker SNX1, then visualised with widefield immunofluorescence microscopy. The percentage of cells with at least one SNX-1-positive tubular structure >1.2μm in length was quantified in 100 cells per sample, and the results for 3 such experiments were plotted in the corresponding chart. Bars indicate mean ± S.E.M., p-values calculated by one-way ANOVA with Tukey's post-hoc test for repeated measures. Micrograph scale bars = 10 μm.

Figure 4. Human neurons lacking VPS4A exhibit similar endosomal phenotypes to proband fibroblasts. A) CRISPRi-i³N iPSCs with were transduced with a scrambled sgRNA and three separate sgRNAs (G1-G3) directed against VPS4A. Cell lysates were immunoblotted against VPS4A. **B**) Selected lines were treated with doxycycline to induce neuronal differentiation, then blotted against VPS4A 14 days later. GAPDH signal validates equal lane loading. **C**) CRISPRi-i³N iPSCs expressing the guides indicated were differentiated to neurons for 14 days, fixed and labelled for EEA1. The percentage of cells with an EEA1-positive organelle over a nominal cut-off size was visualised by widefield microscopy and quantified in 3 experiments (≥ 100 cells per experimental condition in each repeat). The number of EEA1-positive endosomes per cell was visualised using confocal microscopy and quantified in 3 experiments (≥ 20 cells per experimental condition in each repeat). Quantifications are plotted in the corresponding graphs. **D**) i³Neurons expressing the sgRNAs indicated were fixed and labelled for CD63, then visualised by widefield microscopy. The percentage of cells with a CD63 organelle over a nominal cut-off size was quantified as described for EEA1. **E**) i³Neurons expressing the sgRNAs indicated were fixed and labelled for LAMP1 and cathepsin D, then visualised by widefield microscopy. The percentage of cells that had a LAMP1 or cathepsin D organelle over a nominal cut-off size was quantified as described for EEA1. Bars show mean ± S.E.M., p-values generated by one-way ANOVA with Tukey's correction for multiple testing. Scale bars = 10 μm.

Figure 5. The atypical ESCRT-III protein IST1 accumulates on endosomes in human neurons lacking VPS4A. i[3]Neurons expressing the guides indicated were fixed and labelled for IST1 and EEA1 (**A**) or IST1 and CD63 (**B**), then visualised by confocal immunofluorescence microscopy. The number of IST1 puncta per cell and the percentage of EEA1- or CD63- positive endosomes associated with an IST1 punctum was quantified in 3 experiments per marker (in ≥20 cells per experimental condition in each repeat) and plotted in the corresponding charts. Arrows indicate juxtaposed or co-localised puncta. **C**) i[3]Neurons expressing the guides indicated were fixed and labelled for CHMP6, then visualised by confocal immunofluorescence microscopy. The number of CHMP6 puncta per cell was quantified in 3 biological repeats (≥20 cells per experimental condition in each repeat). Bars indicate mean ± S.E.M., p-values calculated by one-way ANOVA with Tukey's correction for multiple testing. Micrograph scale bar = 10 μm.

Figure 6. Defective VPS4A function affects centrosome numbers and mitotic spindle organization. Confocal microscopy analysis was performed in synchronized skin fibroblasts from subjects with *VPS4A* mutations and control cells. Images are representative of three stages of the cell cycle (**A**), interphase, (**B**), metaphase and anaphase-telophase. Cells were stained using antibodies against pericentrin (centrosome marker) and α-tubulin (microtubules and mitotic spindle); chromosomes with DAPI. Scale bars represent 15 μm. The corresponding graphs show the mean +/- SEM of 6 separate counts (≥25 cells/line each) for a total of 200 cells/line scored. P-values were calculated by one-way ANOVA with Tukey's correction for multiple testing.

Figure 7. *VPS4A* mutations cause aberrant chromosome segregation and alter cell cycle progression. A) Staining performed using a fluorescent probe (anti-lamin A/C green) or Giemsa show a significant increase in micronuclei (arrow), chromosome bridges (arrow) and aneuploidy in proband cells compared to control cells. In experiments to assess micronuclei

and chromosome bridges, graphs show the mean +/- SEM of 5 (micronuclei) or 4 (chromosome bridges) separate counts (200 cells/line each, micronuclei; 250 cells/line each, chromosome bridges) for a total of 1000 cells/line scored. In experiments to assess aneuploidy, graphs show mean +/- SEM of 3 separate counts ($\geq$30 cells/line each) for a total of 100 cells/line scored. **B)** Cell cycle phases of control (top) and probands' (bottom) fibroblasts as measured by BrdU incorporation and propidium iodide (PI) flow cytometry analysis. The upper box identifies cells incorporating BrdU (S phase), the lower left box identifies G0/G1 cells, and the lower right box represents G2/M cells. A representative of three independent experiments is shown. In all experiments, p-values were calculated by one-way ANOVA with Tukey's correction for multiple testing. Graph bars show mean +/- SEM.

Figure 8. Proband fibroblasts have abnormal nuclear envelope morphology, increased DNA damage and abnormal primary cilium morphology. A) An increased number of aberrantly shaped nuclei in fibroblasts carrying the *VPS4A* mutations was observed versus control cells. Staining was performed using anti-lamin A/C and DAPI. Scale bar is 10 µm. **B)** Representative images showing an increase number of γ-H2AX foci in probands' fibroblasts carrying compared to control cells. The staining was performed using γ-H2AX antibody and DAPI. Scale bar is 2.5 µm. In all experiments, mean +/- SEM of 4 separate counts ($\geq$40 cells/line each) for a total of 200 cells/line scored. p-values were calculated by one-way ANOVA with Tukey's correction for multiple testing. Graph bars show mean +/- SEM. **C)** Confocal images showing altered primary cilium morphology in proband fibroblasts compared to control cells. Cells heterozygous for the p.R284G amino acid change show absent cilia with only a visible basal body (dot cilium, zoomed image), whereas cells with the p.R284W substitution show either a dot cilium or occasionally an elongated or normal cilium (zoomed image). Primary cilia are labelled with acetylated α-tubulin, basal bodies and nuclei

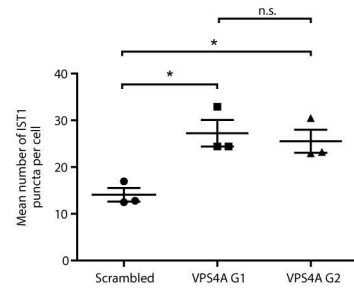are labelled with γ-tubulin and DAPI respectively. Scale bar is 5 µm. 100 cells were analysed for each line over two independent experiments, bars represent the mean.
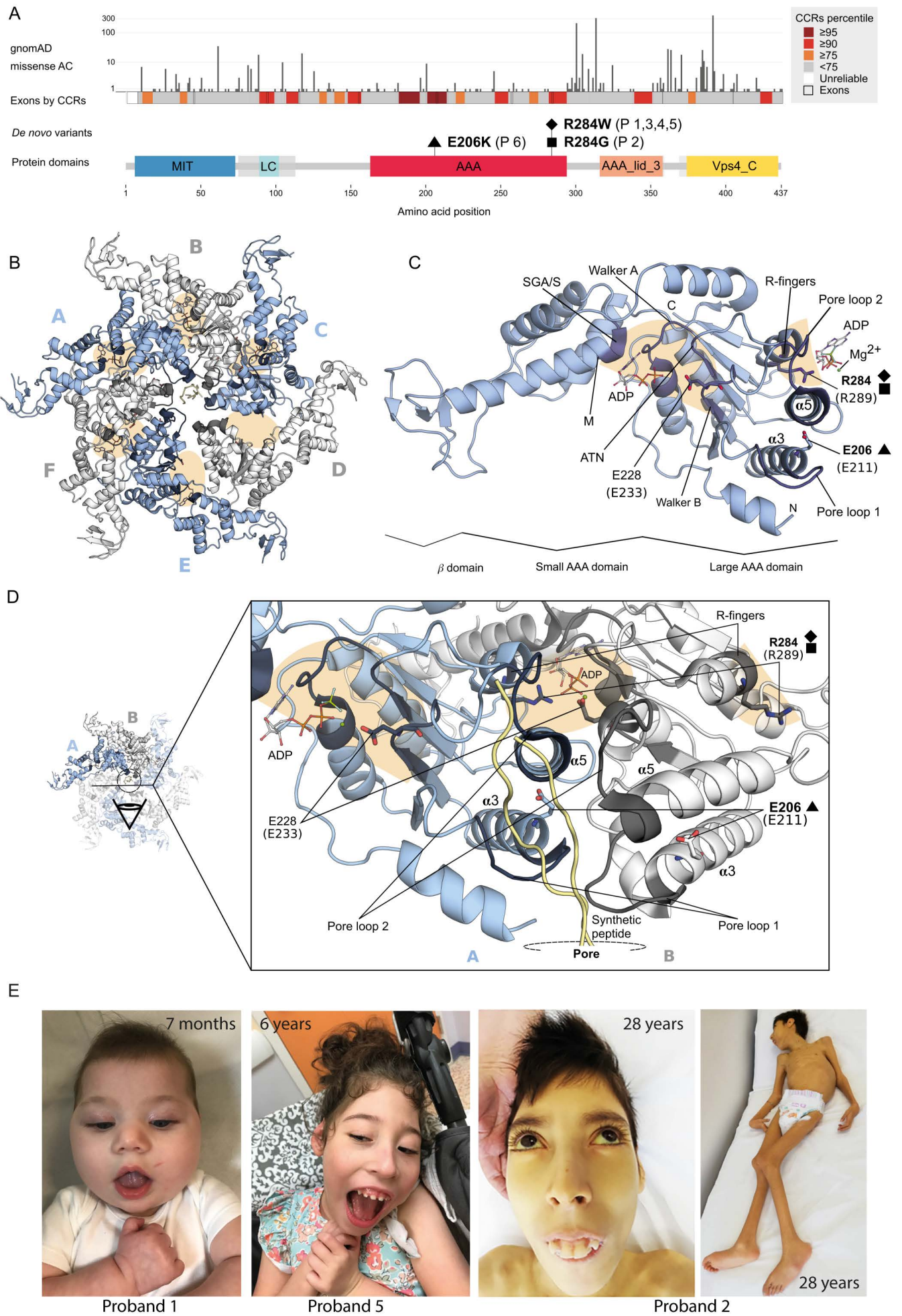
Figure 1
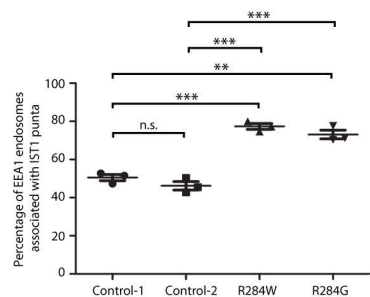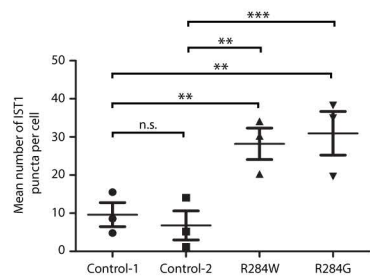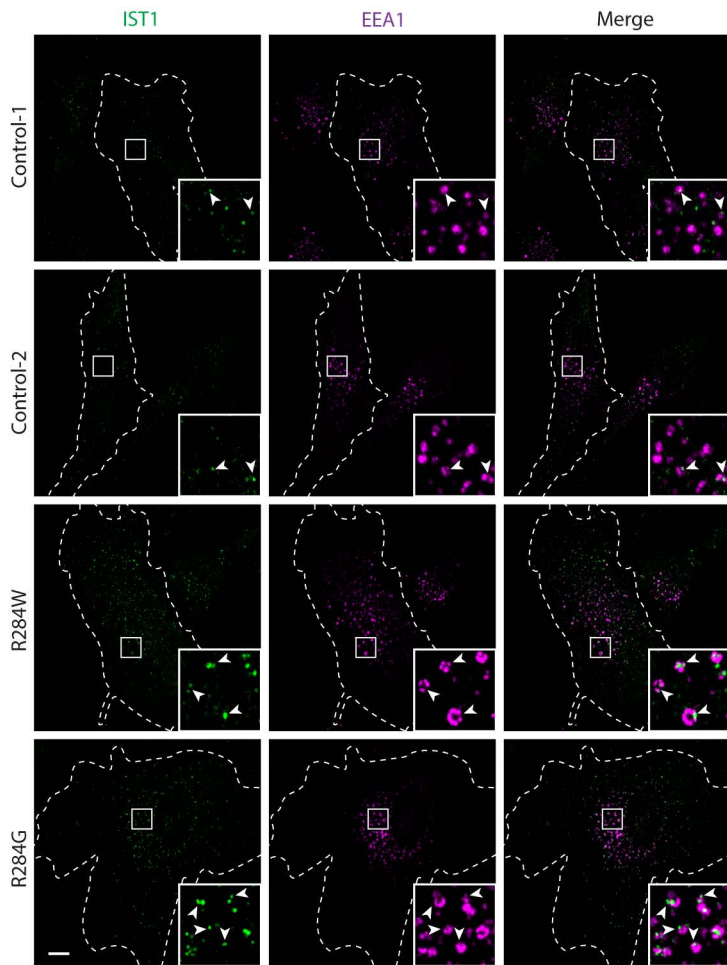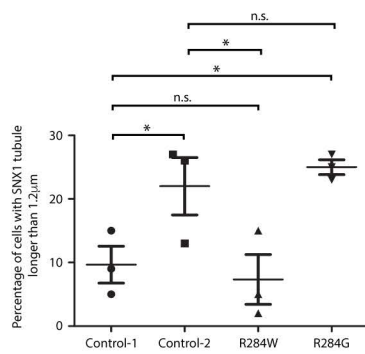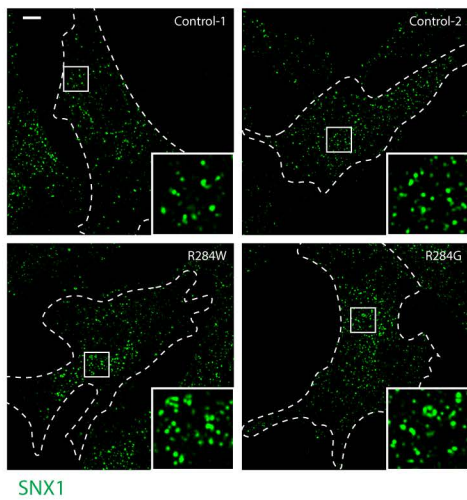
Figure 2

Figure 3

Figure 4

Figure 5

A

	pericentrin	α−tubulin	Dapi	merge
control 3				
R284G				
R284W				

interphase

interphase

% cells with multiple centrosomes

40 — *** *** — 30 — 20 — 10 — 0 —

control 3   R284G   R284W

B

control 3 / R284G / R284W

metaphase

control 3 / R284G / R284W

anaphase/telophase

mitosis

% cells with multiple centrosomes

80 — *** *** — 60 — 40 — 20 — 0 —

control 3   R284G   R284W
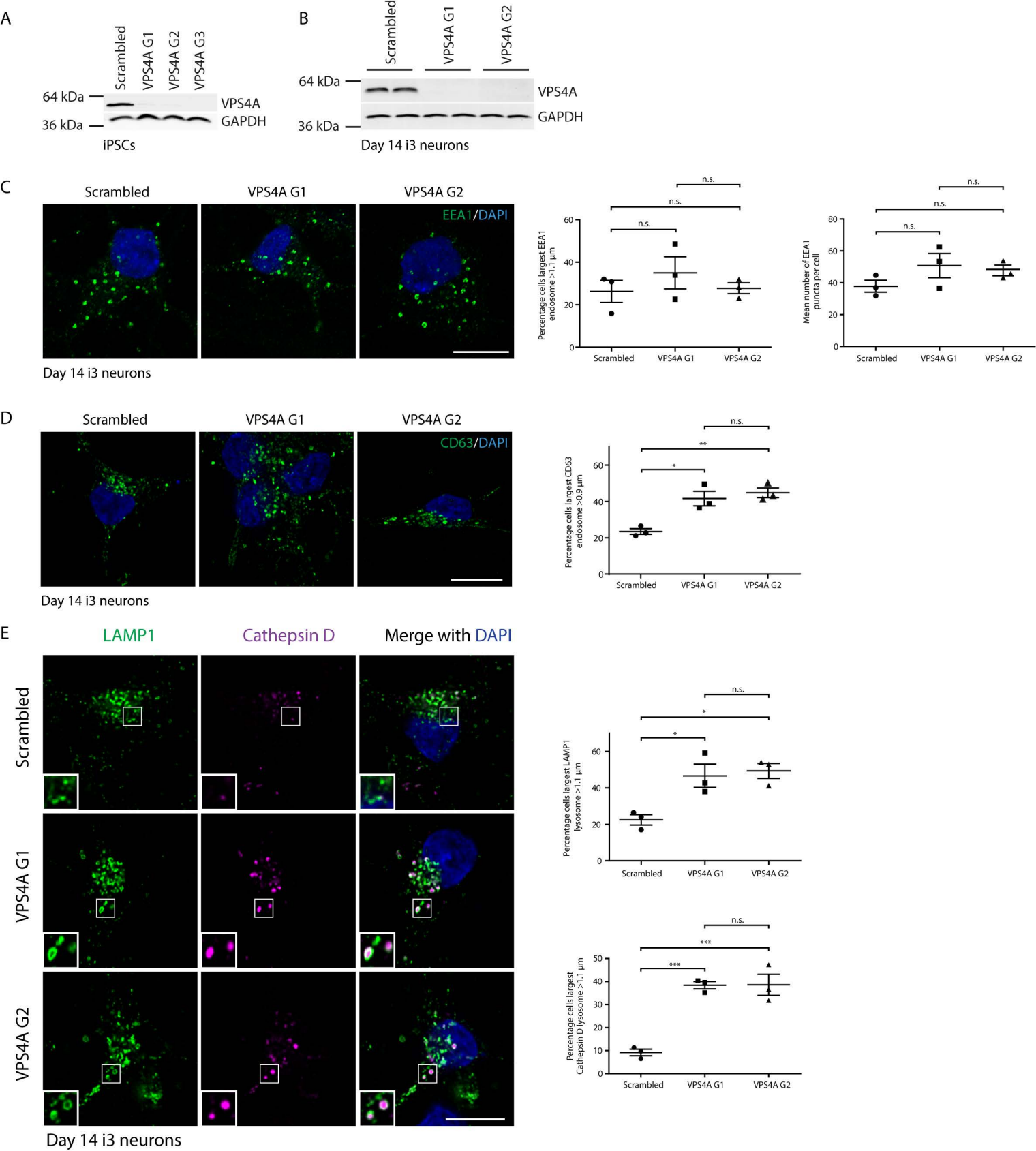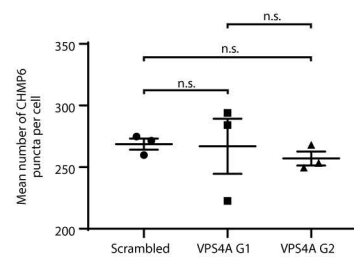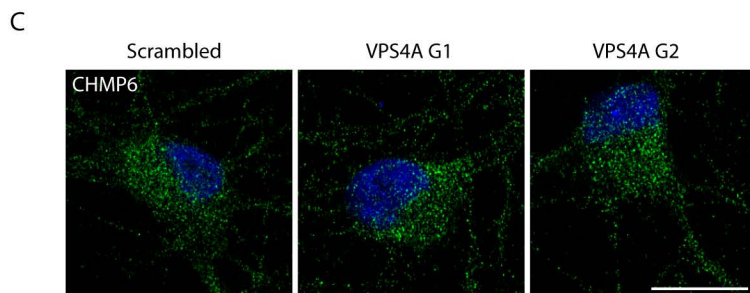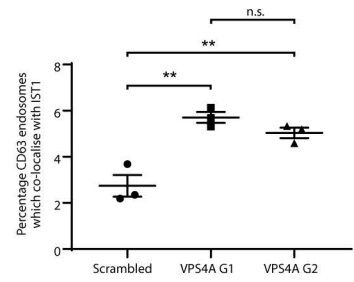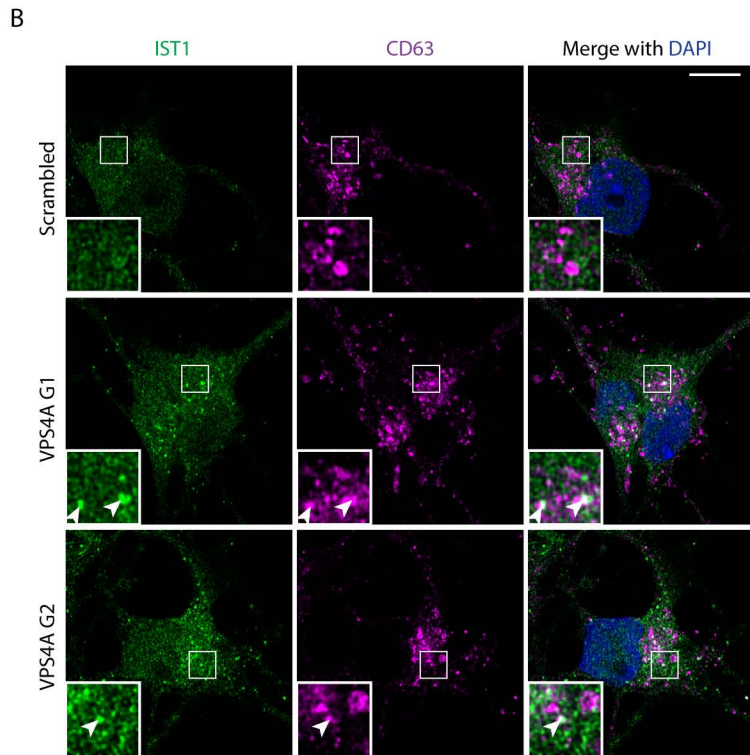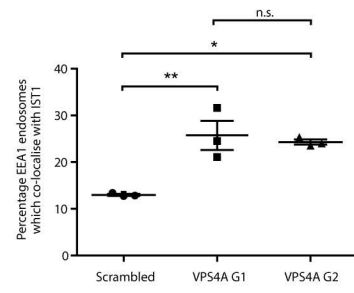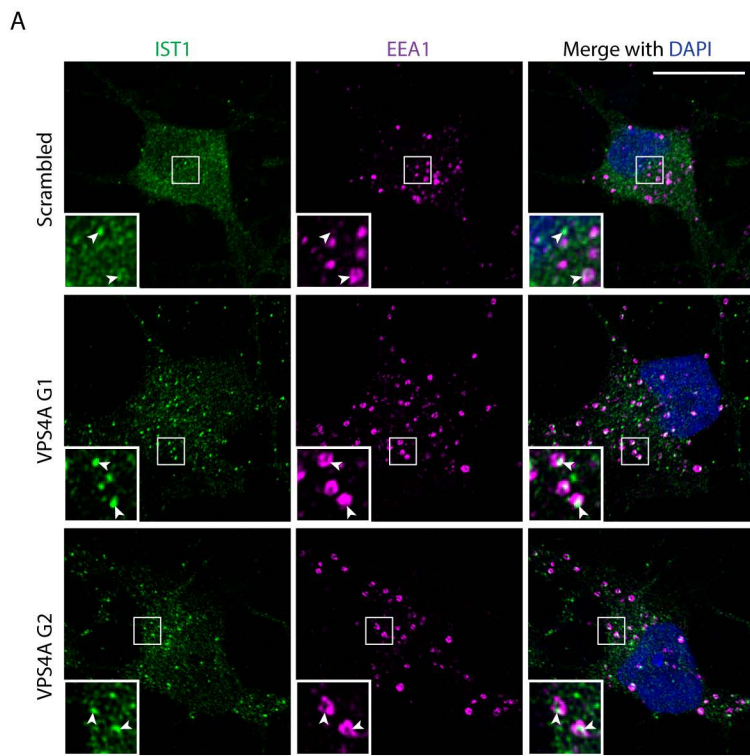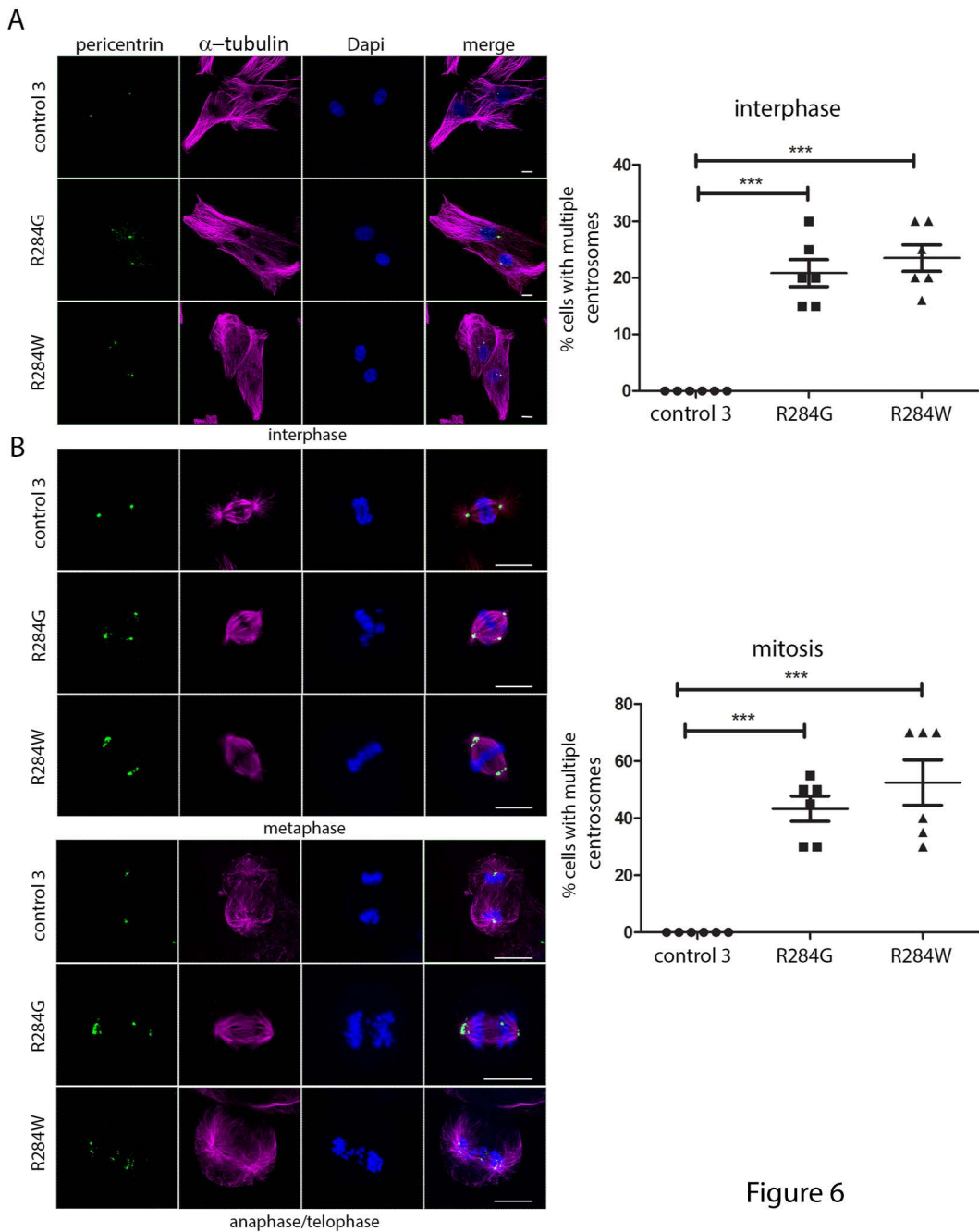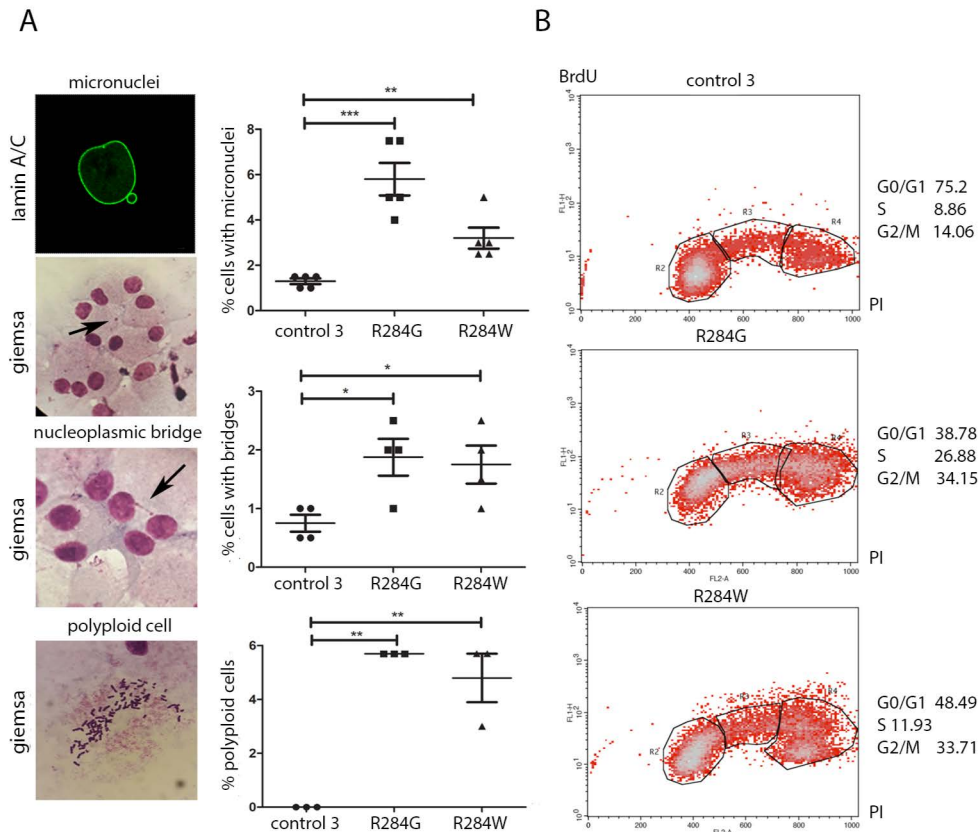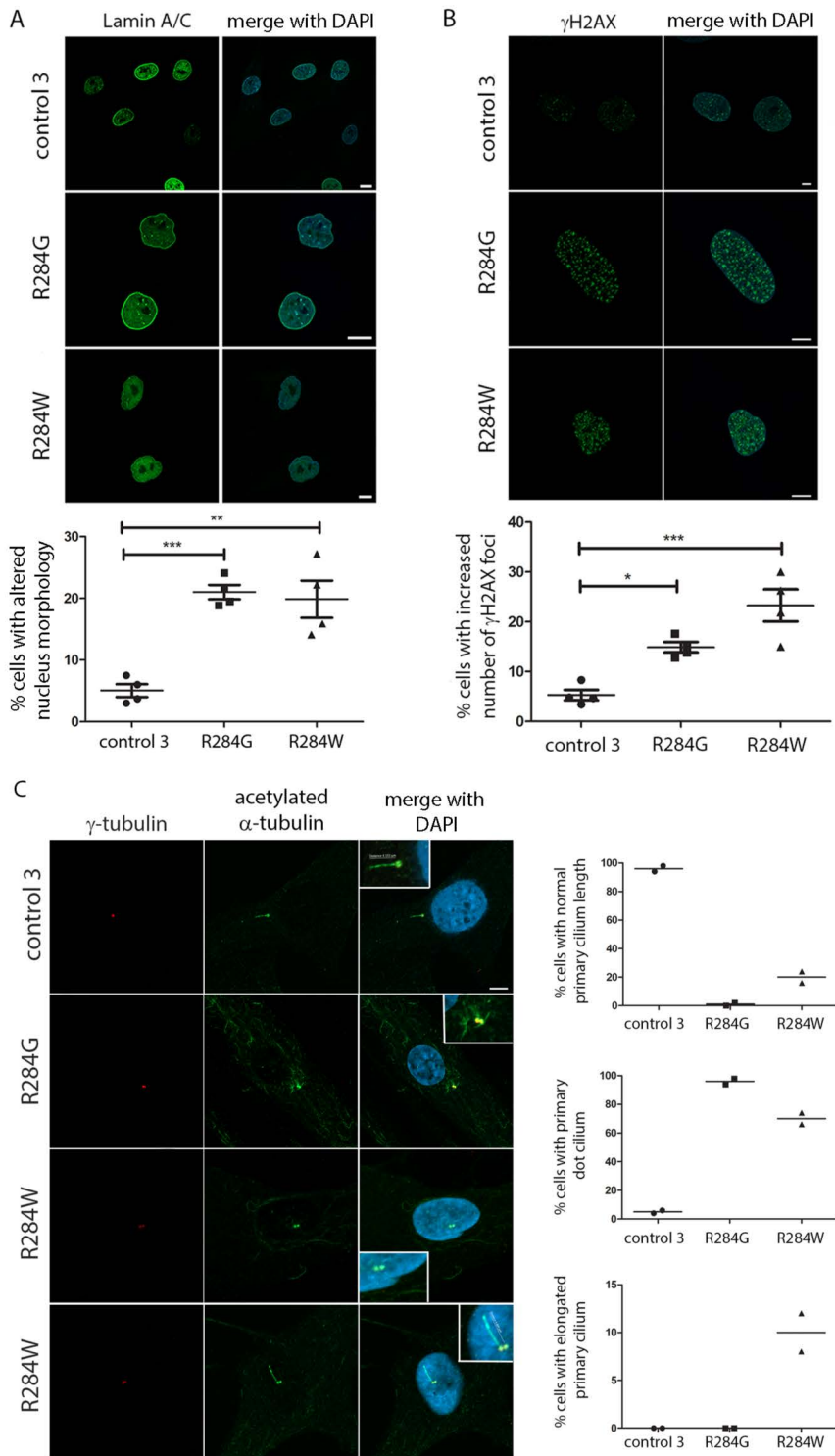
Figure 6

Figure 7

Figure 8

Supplemental Note: Case Reports for representative probands.

<u>Proband 1 (c.850A>T, p.Arg284Trp).</u>

Proband 1 is the 1st child of healthy unrelated parents. Her father was 35 years old and mother 33 years old at the time of her birth. Routine antenatal testing showed a low PAPP-A; a Harmony trisomy screening test was normal. No abnormalities were noted on antenatal ultrasound scan, but in view of the low PAPP-A, serial ultrasound screening was undertaken; the appearances were normal until around the 36 weeks scan, when growth was noted to be small. A semi-urgent caesarean section was undertaken in view of the growth and breech presentation; she was born with birthweight of 2310g (Z -2.8) with a head circumference of 31.4cm (Z -2.6) at 37 weeks.

She cried at birth, and did not need any active resuscitation. She would not breast-feed but sucked reasonably well by bottle with expressed breast milk. She failed her newborn hearing test twice, but further testing subsequently confirmed normal hearing.

Parents were concerned about her visual behaviour and that she was not fixing or following at 8 weeks of age. Ophthalmological examination showed significant central and lamellar lens opacities but no microphthalmia or anterior segment abnormalities. Her father at that time was found to have very mild symptomatic bilateral sutural lens opacities. Following cataract removal, fundal examination on the proband showed an abnormal retinal appearance with abnormal atrophic changes at the macula in keeping with a retinal dystrophy, which was confirmed with very poor ERG and VEP amplitudes.

She developed mild symptoms of cow's milk protein intolerance and gastro-oesophageal reflux, which was treated with ranitidine and omeprazole, and started on Nutramigen. Feeding has continued to be a problem; at the age of 2 years she takes no solids orally, and milk is mild given via NGT. She has persistent vomiting and poor weight gain.

Developmental progress has been slow. She started smiling from around 6 months of age, around which time head control was improving; she was beginning to move her head to sounds at 7 months of age. At the age of 2 years, she is able to roll from back to front, and pivot on her back using her legs, but is not able to support her head on her hands when prone. She is not sitting independently. She laughs responsively and is able to attract

parents' attention by laughing. She recognises her parents' voices, and will respond to familiar stories and songs. She has no words, but has some vocalisations.

Sleep pattern is poor. She developed obstructive sleep apnoea, and underwent a tonsillectomy. She takes melatonin and tends to fall asleep easily, but will often wake after 30-60 minutes and then repeatedly throughout the night, sometimes staying awake for several hours.

Examination showed central hypotonia, with hands held in a clenched position. She tends to hold her mouth open with a protruding tongue. Her movements are dyskinetic. She has small hands and feet.

Array CGH, neurometabolic investigations and a TORCH screen were normal. An echocardiogram was reported as normal. NGS of a panel of genes associated with cataracts and retinal dystrophy did not identify any pathogenic changes. She has had an anaemia with haemoglobin of 88 g/l in infancy, then later 83 g/l, but possibly dietary owing to her intake. The blood film stated that the red cells showed anisocytosis.

MRI: Sulci are mildly prominent which in conjunction with microcephaly suggest cerebral volume loss. The corpus callosum is present; it is thin suggesting white matter volume loss. Sylvian fissures are widened anteriorly. Cortical gyration is likely to be within normal limits. Cerebellar vermis and hemispheres are hypoplastic and there is a small posterior fossa. Brain stem is within normal limits.

ERG showed no consistent retinal responses above the level of noise to a range of stimulus intensities.

VEPs showed no consistent pattern reversal cortical responses evident above the level of noise confirming a very degraded pattern.

Proband 2 (c.850A>G, p.Arg284Gly).

An 8-month-old male presented with a phenotype characterized by microcephaly (-5 SD), congenital cataract, large ears, long palpebral fissures, strabismus, retrognathia with wide mandibular angle, single transverse palmar crease, bilateral clubfoot, hypertonia, global developmental delay. The pregnancy was uncomplicated. He was born to partners who were cousins, at 39 weeks of gestation, by elective secondary caesarean section. Auxologic

parameters were normal, Apgar score was 3 at 1 minute and 9 at 5 minutes after birth, orotracheal intubation was not performed.

Four days after birth he developed severe haemolytic anaemia requiring transfusion. Haemolytic episodes recurred leading to liver and spleen enlargement, common causes of anaemia and haemolisis were ruled out. Afterwards the proband's medical history was significant for severe oromotor disability and failure to thrive with weight and length < -5 SD, parents declined artificial nutrition. He presented with hypovision and moderate bilateral sensorineural deafness.

At 18 months psychomotor development delay was confirmed, cerebral MRI revealed corpus callosum hypoplasia and severe cerebellar hypoplasia. Electroencephalography detected abnormal brain electrical activity; the proband didn't present with clinical seizures. The neurological pattern got worse and he developed severe intellectual disability and total dependence from caregiver.

At the last clinical evaluation, 3 months before death, he presented with severe malnutrition, microcephaly, large ears, long palpebral fissures, strabismus, long oval face, long philtrum, gingival hypertrophy, exposed upper incisors, retrognathia with wide mandibular angle, single transverse palmar crease, flexion deformity of wrist, elbow, knee with popliteal pterigium, bilateral clubfoot, scoliosis of the spine and hypogenitalism. He also showed yellow sclera, suggestive of liver involvement. He died at the age of 29 years from respiratory failure secondary to pneumonia.

Proband 3 (c.850A>T, p.Arg284Trp).

The proband was the second child to unrelated Caucasian parents. He was born at term following an uncomplicated pregnancy and discharged home at 6 hours of age. He was readmitted within 24 hours with vomiting and drowsiness. He was investigated for sepsis and treated with antibiotics. Microcephaly and hypotonia were noted on that admission. He continued to vomit and had failure to thrive. Feeding became a significant issue and never was successfully established – he had a PEG inserted but vomiting remained problematic. He subsequently had a fundoplication and a jejunal tube placed – this helped his symptoms but he continued to retch. He made very little in the way of developmental progress – he could hold his head in the midline and responded to his parents voice; he never fixed and

followed. From the beginning, he had episodes of arching and irritability – initially thought to be due to significant gastro-oesophageal reflux. With time, these evolved into dystonic and dyskinetic movements. As his condition progressed, he was diagnosed with 'salt and pepper' retinitis, cataract and liver dysfunction. He had progressively enlarging liver and mild conjugated hyperbilirubinaemia and abnormal liver function tests. He did not develop liver failure. Prior to his death he had short episodes of gazing in one direction associated with limb movements but was never formally diagnosed with seizures. He died at 26 months of age.

He was extensively investigated from a neurometabolic point of view and his positive findings included

1. MRI - bilateral frontal polymicrogyria and Pontocerebellar hypoplasia
2. CK – raised on 2 occasions to 1500, normal on other occasions
3. Muscle Biopsy – said to show features of myopathy
4. Liver Biopsy – microvesicular steatosis and haemosiderosis
5. Respiratory chain analysis – normal
6. Microarray 17p11.2 del - VUS paternally inherited
7. Cardiff Cortical malformation gene panel– no significant findings

Additional findings at Post mortem included

1. Skeletal survey showed 'hair on end' appearance to outer table of skull
2. Moderate abdominal ascites
3. Malrotation and volvulus - Appendix, caecum and proximal ascending colon in left upper quadrant

The clinical impression was always of a rare neuro metabolic disorder.

Author List for Genomics England Research Consortium

Ambrose J. C. [1], Arumugam P.[1], Baple E. L. [1], Bleda M. [1], Boardman-Pretty F. [1,2], Boissiere J. M. [1], Boustred C. R. [1], Brittain H.[1], Caulfield M. J.[1,2], Chan G. C. [1], Craig C. E. H. [1], Daugherty L. C. [1], de Burca A. [1], Devereau, A. [1], Elgar G. [1,2], Foulger R. E. [1], Fowler T. [1], Furió-Tarí P. [1], Hackett J. M. [1], Halai D. [1], Hamblin A.[1], Henderson S.[1,2], Holman J. E. [1], Hubbard T. J. P. [1], Ibáñez K.[1,2], Jackson R. [1], Jones L. J. [1,2], Kasperaviciute D. [1,2], Kayikci M. [1], Lahnstein L. [1], Lawson K. [1], Leigh S. E. A. [1], Leong I. U. S. [1], Lopez F. J.[1], Maleady-Crowe F. [1], Mason J. [1], McDonagh E. M. [1,2], Moutsianas L. [1,2], Mueller M. [1,2], Murugaesu N. [1], Need A. C. [1,2], Odhams C. A. [1], Patch C. [1,2], Perez-Gil D. [1], Polychronopoulos D. [1], Pullinger J. [1], Rahim T. [1], Rendon A. [1], Riesgo-Ferreiro P.[1], Rogers T. [1], Ryten M. [1], Savage K. [1], Sawant K. [1], Scott R. H. [1], Siddiq A. [1], Sieghart A. [1], Smedley D. [1,2], Smith K. R. [1,2], Sosinsky A. [1,2], Spooner W. [1], Stevens H. E. [1], Stuckey A. [1], Sultana R. [1], Thomas E. R. A. [1,2], Thompson S. R. [1], Tregidgo C. [1], Tucci A. [1,2], Walsh E. [1], Watters, S. A. [1], Welland M. J. [1], Williams E. [1], Witkowska K. [1,2], Wood S. M. [1,2], Zarowiecki M.[1]

1. Genomics England, London, UK
2. William Harvey Research Institute, Queen Mary University of London, London, EC1M 6BQ, UK.

Supplemental Methods

EGFR degradation assay

EGFR degradation assays were performed as described previously.[32] Briefly, proband fibroblasts were serum starved overnight before the addition of 100 ng/mL EGF (Calbiochem) in the presence of 10 μg/mL cyclohexamide (Sigma-Aldrich). Cells were lysed at 0, 30, 90 and 180 minute time-points, then analysed by western blotting.

Electron Microscopy

Fibroblasts were seeded to Thermanox (Thermo Fisher Scientific) plastic coverslips and fixed with 2% PFA, 2.5% glutaraldehyde, and 0.1 M cacodylate buffer (pH 7.2). Cells were post-fixed with 1% osmium tetroxide:1.5% potassium ferricyanide before being incubated with 1% tannic acid to enhance contrast. Cells were dehydrated using increasing percentages of ethanol before being embedded onto EPON stubs or beam capsules. Resin was cured overnight at 65°C, and coverslips were removed using a heat-block. Ultrathin (50- to 70-nm) conventional sections were cut using a diamond knife mounted to a Reichart ultracut S ultramicrotome. Sections were collected onto copper grids stained using lead citrate. Sections were viewed on a FEI Tecnai transmission electron microscope at a working voltage of 80 kV.
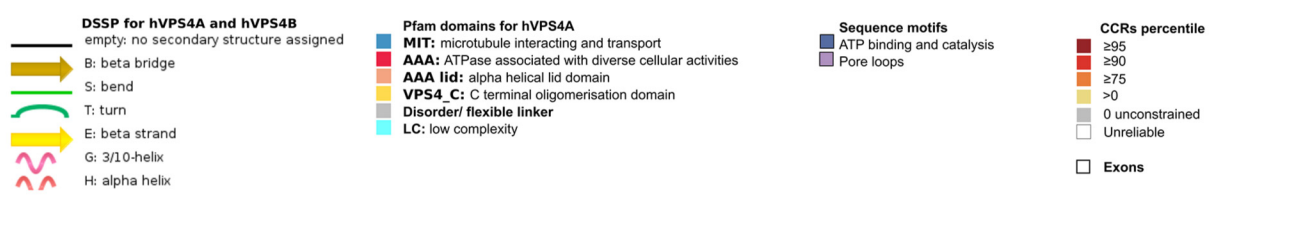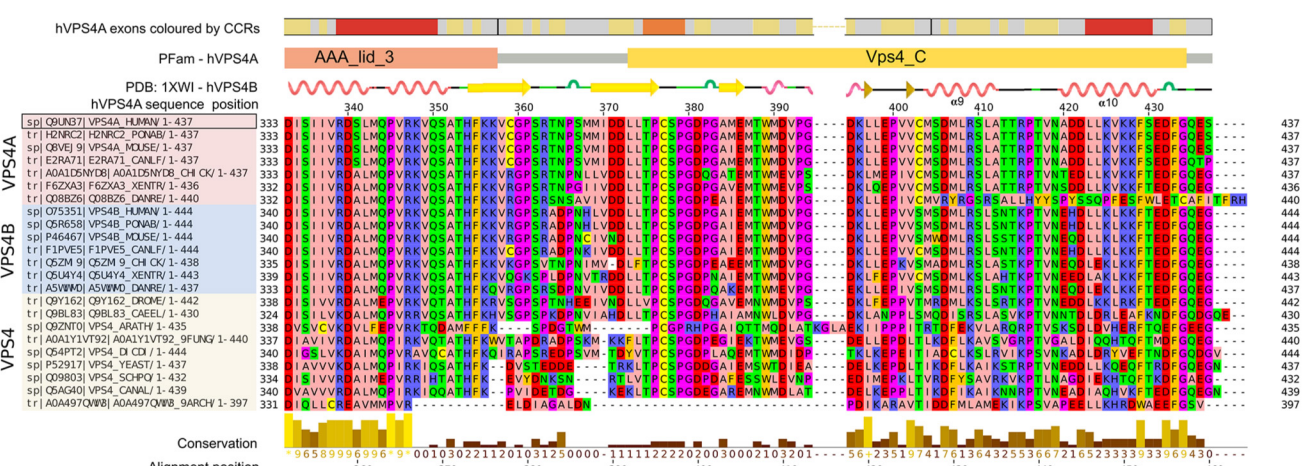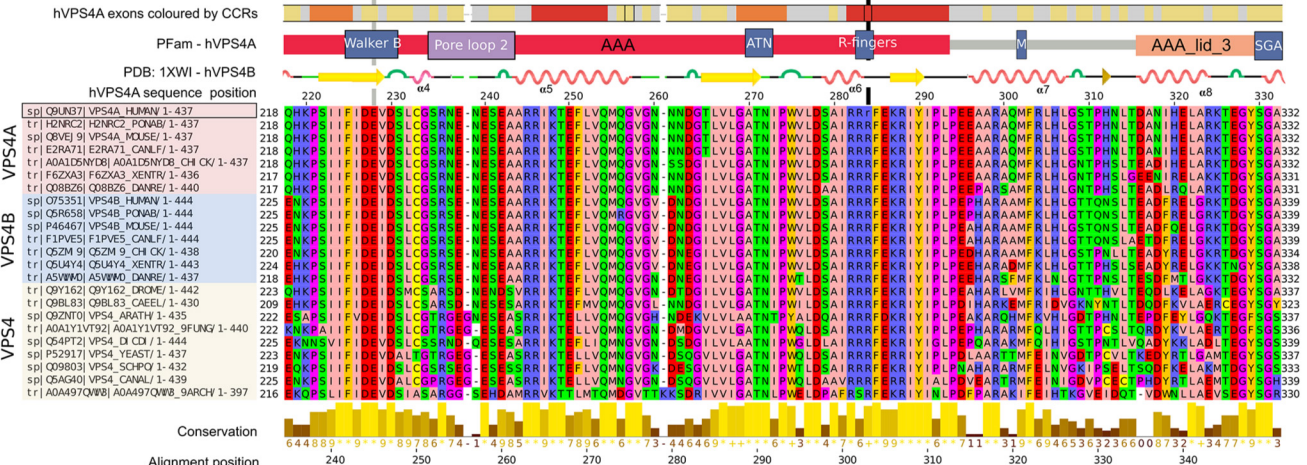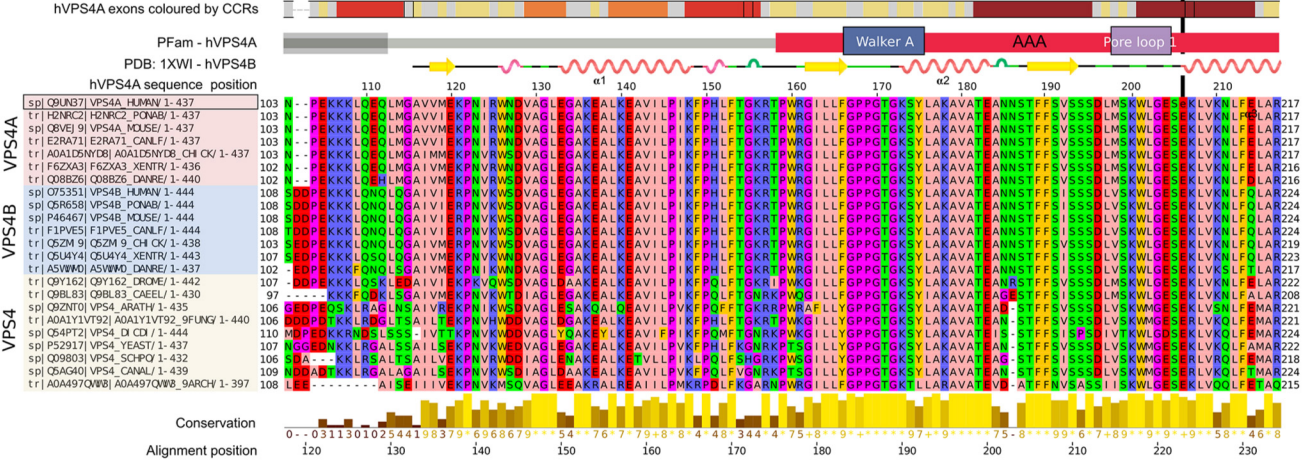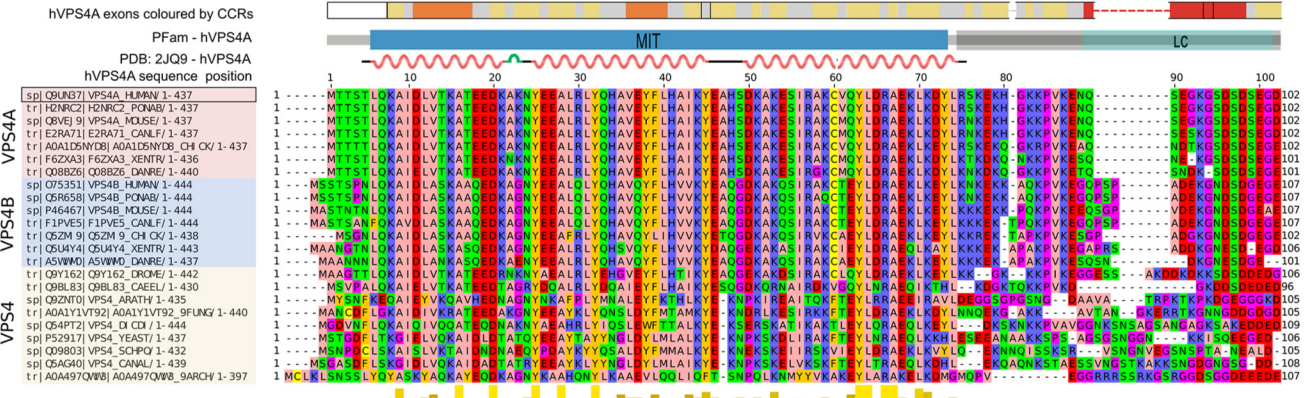
Figure S1

Figure S1. Multiple sequence alignment of VPS4 proteins from representative species.
The novel *de novo* missense variants in VPS4A are represented in the corresponding columns of the alignment, using the same symbols as in Figure 1. The top track depicts CCRs percentiles for human VPS4A (hVPS4A). The protein domains depicted in the second track are based on hVPS4A (UniProtKB entry Q9UN37). The third track shows secondary structural elements based on PDB structures for different regions of hVPS4A or human VPS4B (hVPS4B). In the multiple sequence alignment residues are coloured according to their physicochemical properties (Jalview color scheme). PONAB= orangutan; MOUSE= mouse; CANLF= dog; CHICK= chicken; XENTR= frog; DANRE= zebrafish; DROME= drosophila; CAEEL= worm; ARATH= arabidopsis; 9FUNG= fungus; DICDI= slime mold; SCHPO= yeast; CANAL= Candida albicans; 9ARCH= heimdallarchaeota. The bottom track shows amino acid conservation.

A

B

Pore loop 2

ADP

R284
(R289)

α5

ADP

E228
(E233)

E206 ▲
(E211)

α3

Pore loop 1

Synthetic
peptide

Linker

Pore loop 2

R284
(R291)

α5

ADP/ATP

Mg²⁺

E228
(E235)

E206 ▲
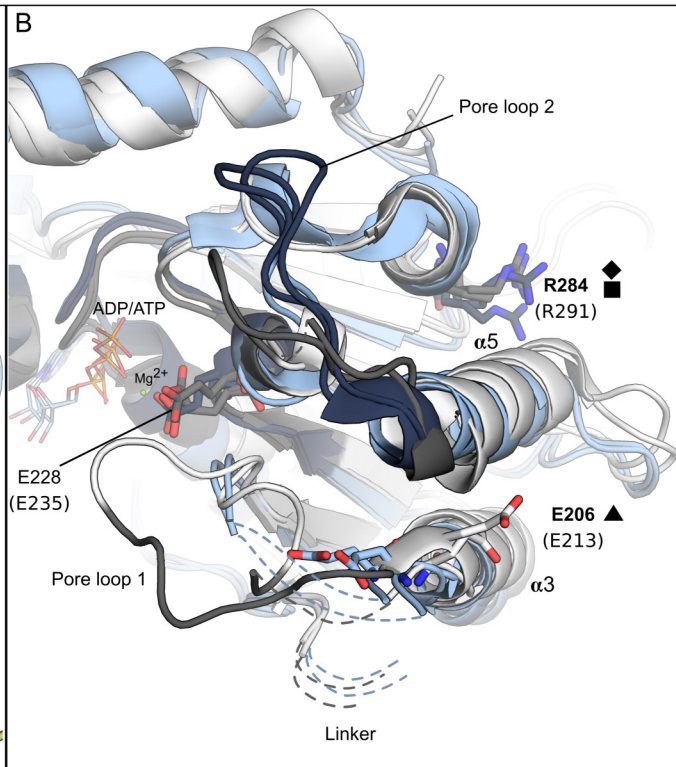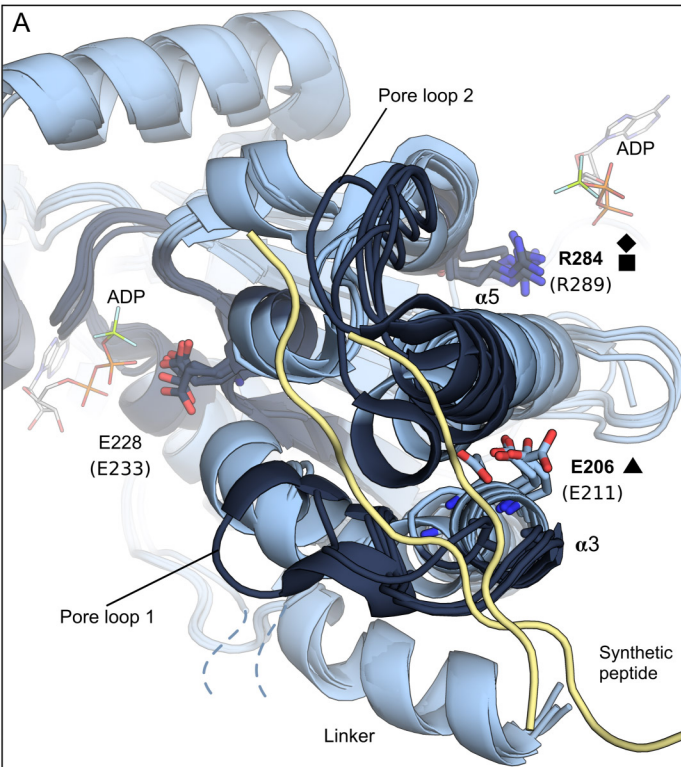(E213)

α3

Pore loop 1

Linker

Figure S2

Figure S2. Protein structural superposition of the ATPase domain of A) the 6 chains of the VPS4 hexamer from yeast (PDB ID: 6OO2) and B) the monomeric VPS4B from human (PDB ID: 1XWI) and mouse (PDB ID: 2ZAM, 2ZAO, 2ZAN). In (**B**), chains in white correspond to apo structures and chains in blue have ADP or ATP bound. The superposition of all chains was done using the human structure as reference. In yellow is the synthetic peptide that shows how the ESCRT-III proteins would translocate through the pore. Residues with missing coordinates are represented with dashed lines. The flexible linker connector is missing in human and mouse structures (**B**) but can be partially observed as α-helix in four chains of yeast VPS4 structure (**A**).

A

Proband 1
7 months
24 months

Proband 5
6 years

Proband 2
8 months
28 years
28 years
28 years
28 years
8 months
28 years

B

3 months
HAR
AFR
FHL
FPL
ST: 4 mm
SP: 4.5 mm
WL: 655
WW: 1310

3 months
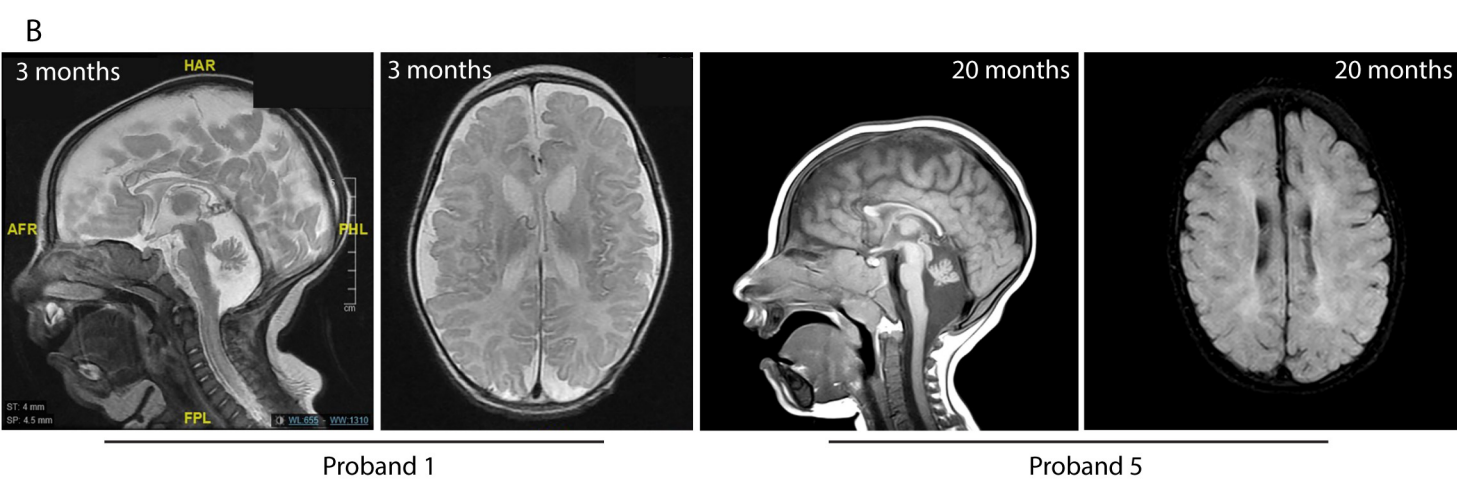
20 months

20 months

Proband 1

Proband 5

Figure S3

Figure S3. Additional clinical images of probands. **A**) Photographs showing probands 1, 2 and 5. Note common features of microcephaly, long palperal fissures, strabismus, long relatively smooth philtrum and broad and arched eyebrows. In the older probands, large ears, long oval face, gingival hypertrophy, exposed upper incisors and retrognathia with wide mandibular angle are common features. Proband 2 also had jaundice, a single transverse palmar crease, flexion of wrist, elbow, knee with popliteal pterigium, bilateral clubfoot and scoliosis. **B**) MRI images of probands 1 and 5. Proband 1: Sagittal and axial T2 MRI images, Proband 5, left is sagittal T1 MRI image and right is T2 flair axial image. Abnormal features in both include thinning of the corpus callosum, atrophy or under-development of the cerebellum, pontine hypoplasia and white matter volume loss. In proband 1 there is extensive dysgyria and in proband 5 there is periventricular gliosis and scalloping of the lateral ventricles.
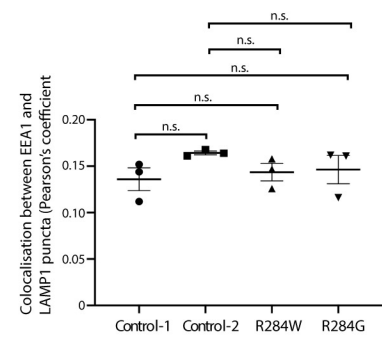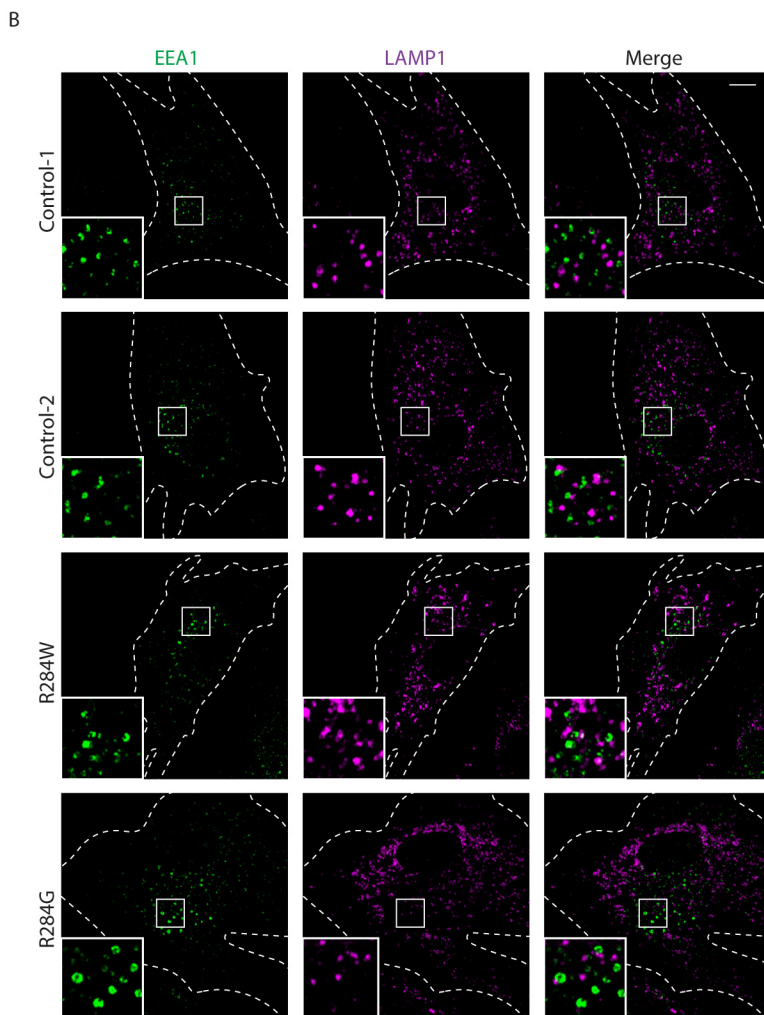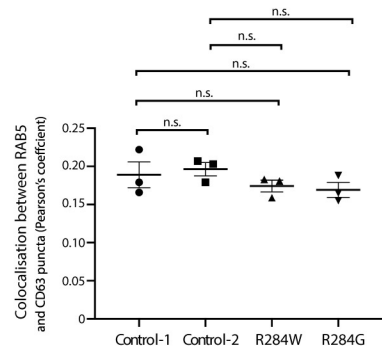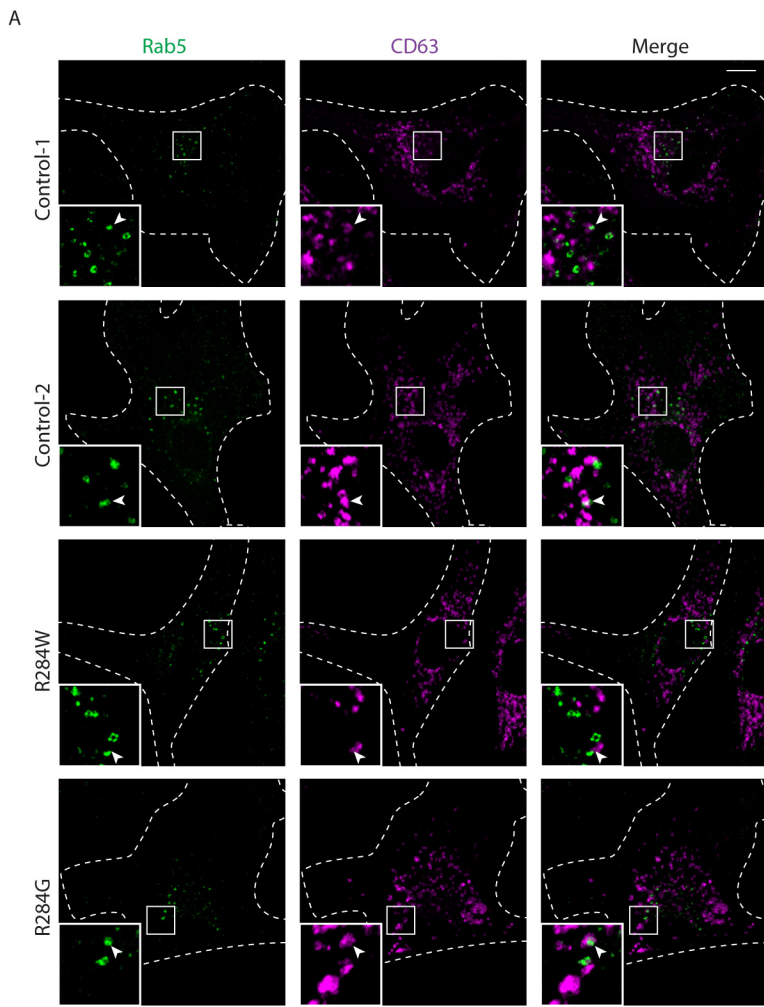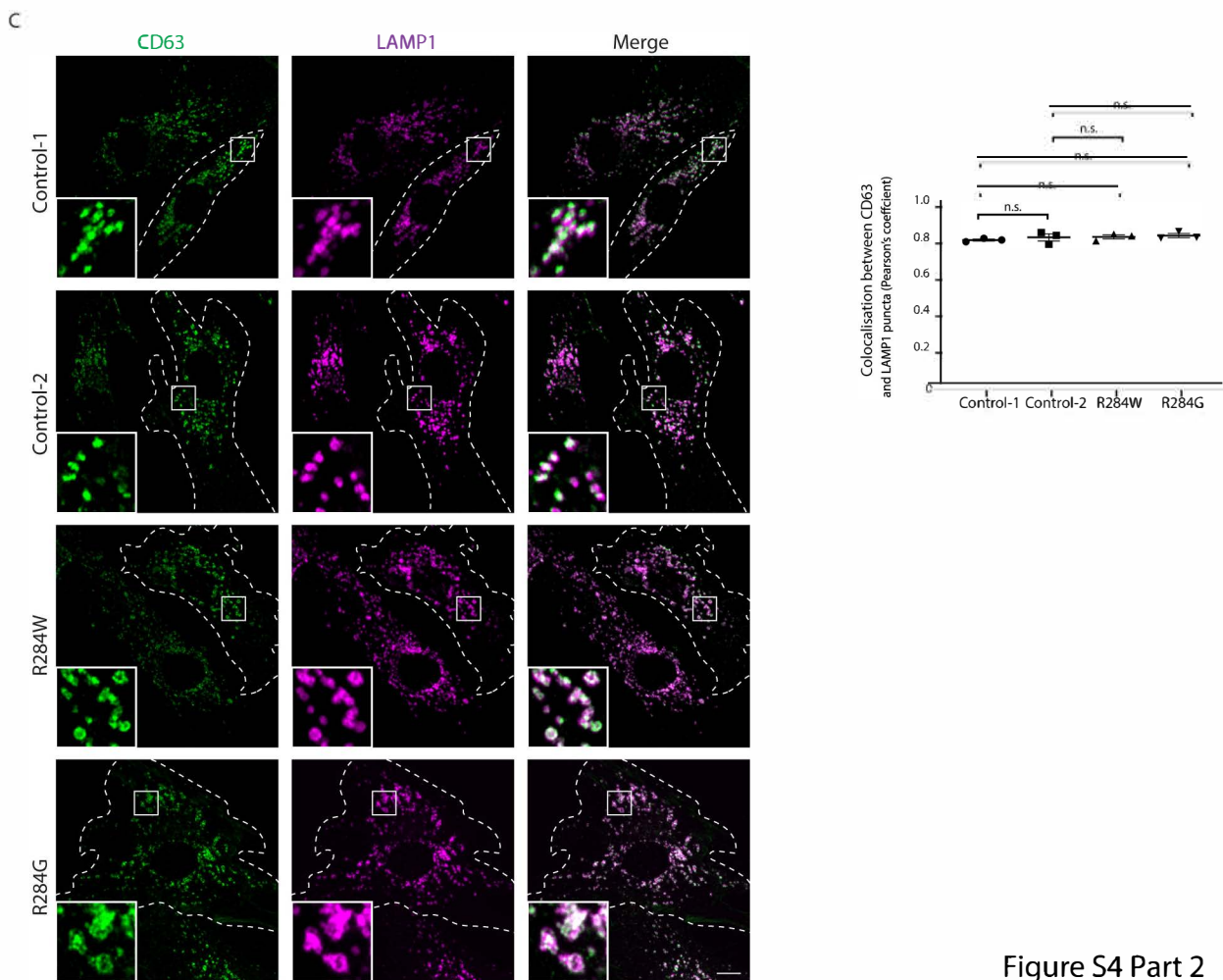
A

B

Figure S4 Part 1

Figure S4 Part 2

Figure S4. VPS4A proband fibroblasts show no endosomal compartment content mixing. Cultured fibroblasts from control subjects and the probands indicated were fixed, labelled with the early endosomal marker RAB5 and CD63 (**A**), EEA1 and LAMP1 (**B**) and CD63 and LAMP1 (**C**), then visualised by confocal immunofluorescence microscopy. Colocalisation was measured using Pearson's co-efficient (in 20 cells in each repeat), and the result of n=3 biological repeats for each set of markers is quantified in the corresponding charts. Bars indicate mean ± S.E.M., p-values were calculated by one-way ANOVA with Tukey's post-hoc test for repeated measures. Micrograph scale bars = 10 μm.
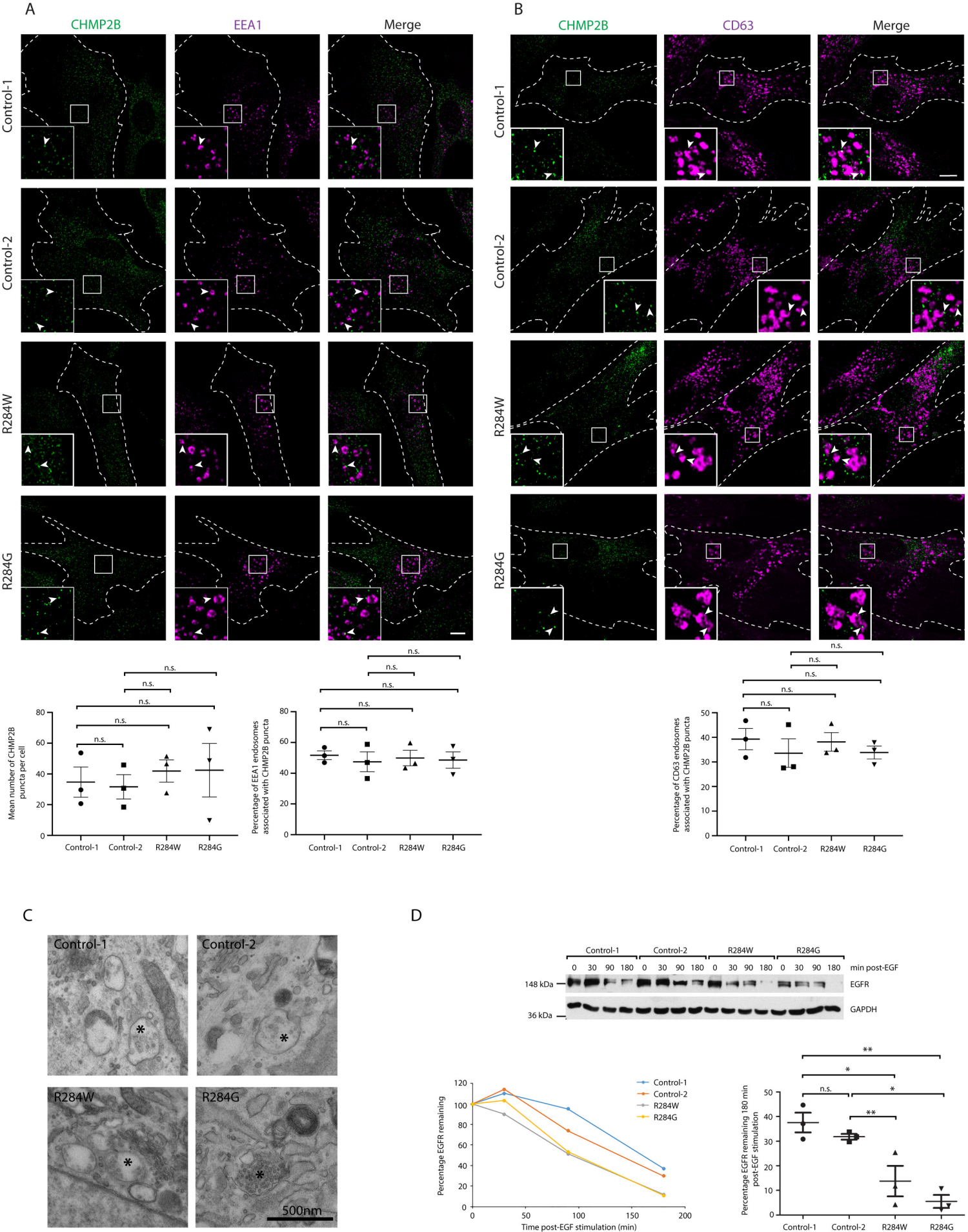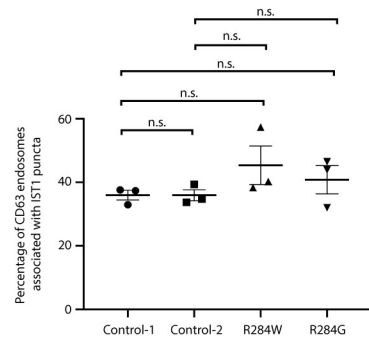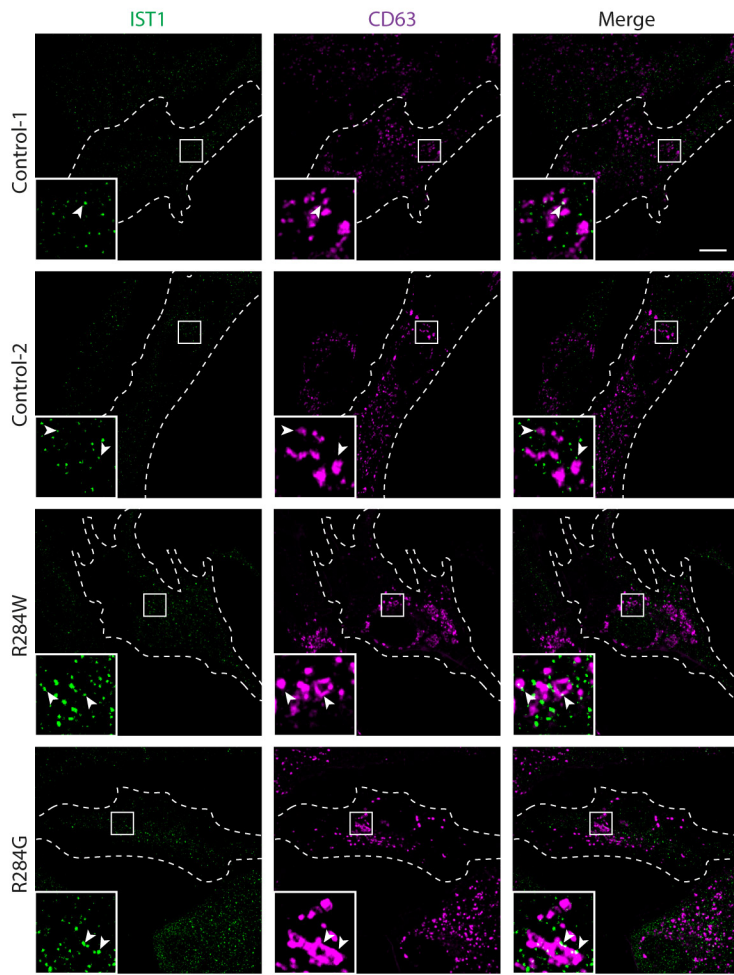
Figure S5

Figure S5. Proband fibroblasts show no defects in endosomal functions of the core ESCRT-III complex. A-B) Cultured fibroblasts from the control subjects or the probands indicated were fixed, labelled against EEA1 (**A**) or CD63 (**B**) and the core ESCRT-III complex member CHMP2B, then visualised by confocal immunofluorescence microscopy. In (**A**) the number of CHMP2B puncta and the percentage of EEA1-positive endosomes associated with a CHMP2B punctum was quantified in 3 experiments (5 cells per experimental condition in each repeat) and plotted in the graphs beneath the images. In (**B**) the percentage of CD63-positive endosomes associated with a CHMP2B punctum was quantified in 3 experiments (in 5 cells per experimental condition in each repeat) and plotted beneath the images. Micrograph scale bar = 10 μm. Arrows indicate juxtaposed or co-localised puncta. **C**) Fibroblasts derived from the subjects indicated were imaged for transmission electron microscopy. MVBs containing ILVs were evident in all cases (indicated by *). Scale bar = 500 nm. **D**) Fibroblasts from probands and controls were stimulated with EGF, lysed at the times indicated, then immunoblotted to monitor EGFR degradation. The line chart on the left shows EGFR quantification normalised to the initial amount of EGFR for a representative experiment, while the plot on the right shows the percentage of EGFR remaining at the 180 min time point for n=3 such experiments. In all plots, bars indicate mean ± S.E.M., p-values calculated by one-way ANOVA with Tukey's post-hoc test for repeated measures.
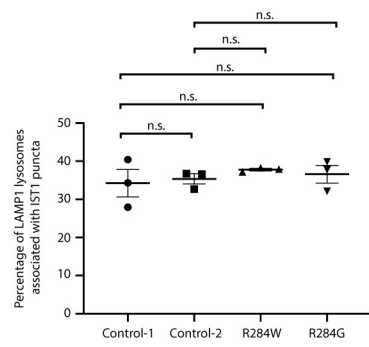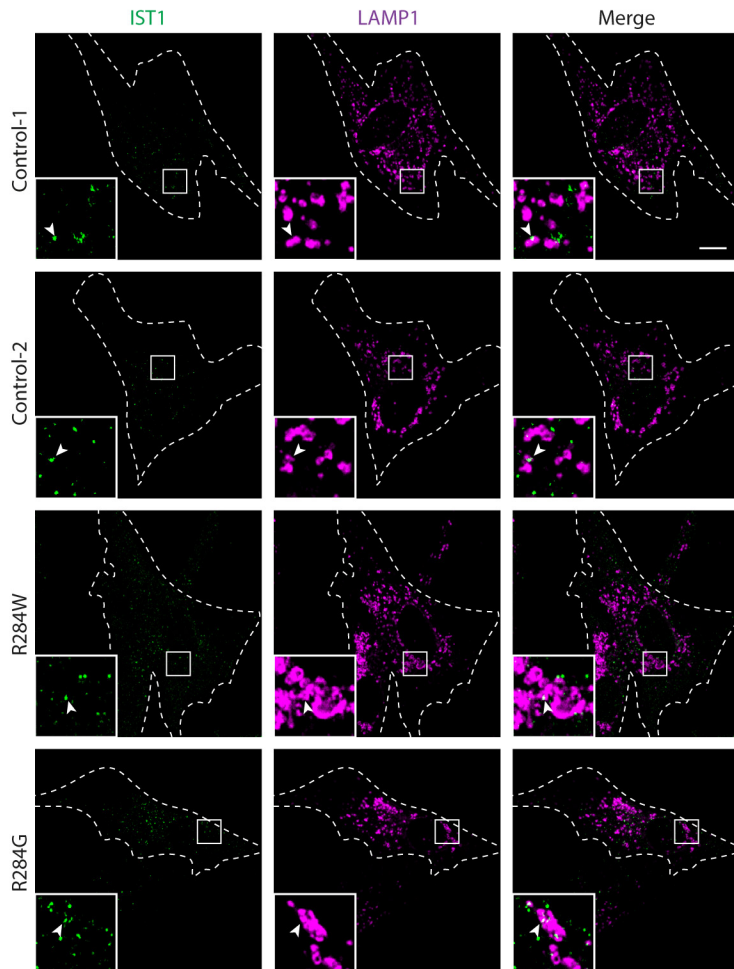
Figure S6

Figure S6. No increased recruitment of IST1 to late endosomes or lysosomes in proband fibroblasts. Cultured fibroblasts from the control subjects and the probands indicated were fixed and labelled for **A**) IST1 and CD63 or **B**) IST1 and LAMP1. The percentage of CD63 or LAMP1-positive endosomes associated with an IST1 punctum was quantified in 3 experiments per marker (in 5 cells per experimental condition in each repeat) and plotted in the corresponding charts. Arrows indicate juxtaposed or co-localised puncta. Bars indicate mean ± S.E.M., p-values were calculated by one-way ANOVA with Tukey's post-hoc test for repeated measures. Micrograph scale bar = 10 μm.
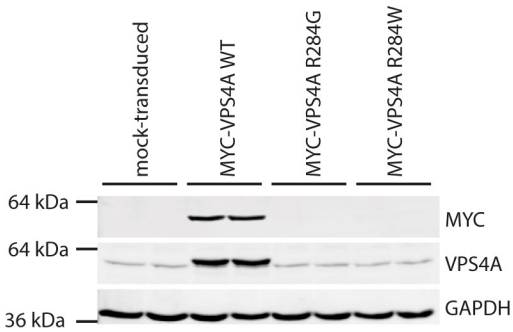
A

64 kDa — MYC

64 kDa — VPS4A

36 kDa — GAPDH

mock-transduced | MYC-VPS4A WT | MYC-VPS4A R284G | MYC-VPS4A R284W

B

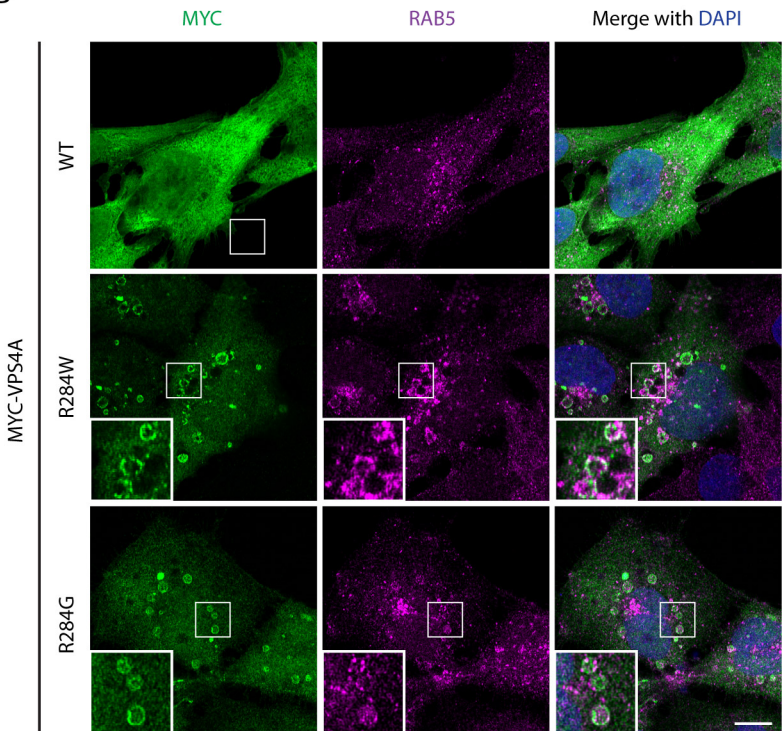MYC | RAB5 | Merge with DAPI

MYC-VPS4A

WT

R284W

R284G

Figure S7

Figure S7. Expression of VPS4A containing disease-associated sequence changes causes the development of vacuolar endosomal structures in iPSCs. A) I³ iPSCs were lentivirally transduced with expression constructs for myc-tagged wild-type VPS4A, or forms of VPS4A containing the p.R284G or p.R284W disease-associated changes. Cell lysates were then immunoblotted with the antibodies indicated. GAPDH immunoblotting serves as a control to verify equal protein loading in each lane. **B**) Transduced cells were also fixed and labelled with antibodies against the myc epitope and RAB5, then visualised by confocal immunofluorescence microscopy. Examples of rare cells containing large vacuolar endosomal structures are shown in the inset higher magnification boxes. Micrograph scale bar = 10 μm.
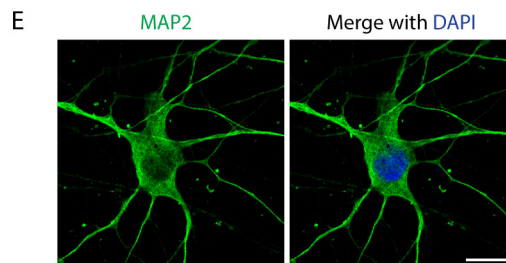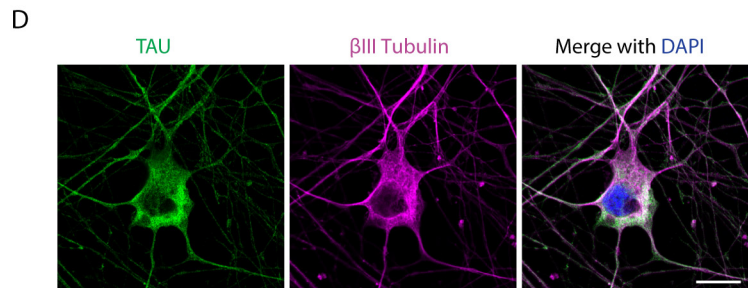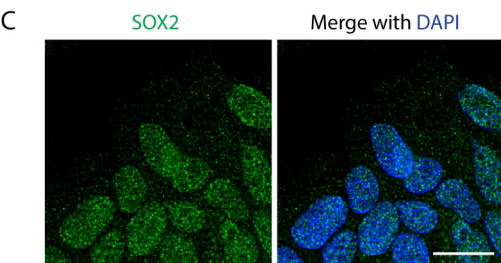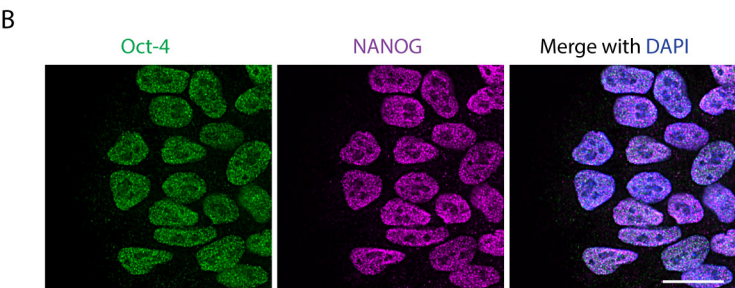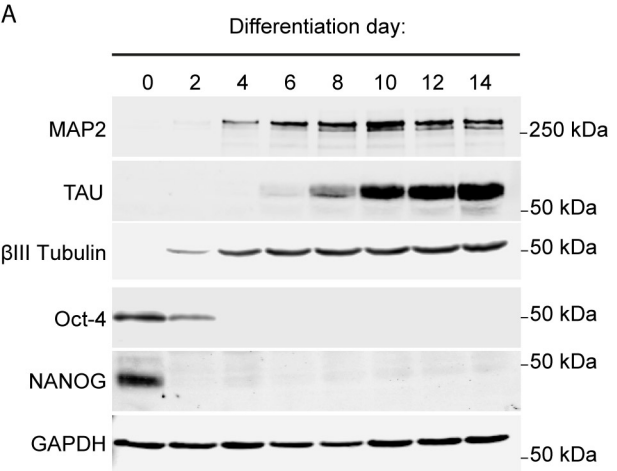
Figure S8

Figure S8. Time course experiment demonstrating loss of pluripotency and gain of neuronal characteristics in i³N iPSCs and neurons. A) i³N iPSCs were cultured in the presence of doxycycline for 3 days. Cell lysates were then made at the time points indicated and blotted against the neuronal differentiation markers MAP2, Tau and βIII-tubulin, as well as the pluripotency markers Oct-4 and NANOG. GAPDH immunoblotting serves as a control to validate equal protein loading across lanes. **B-E**) i³N iPSCs (**B** and **C)** and i³Neurons 14 days post induction of differentiation (**D** and **E**) were fixed and processed for confocal immunofluorescence microscopy with the pluripotency (Oct-4, NANOG and SOX2) and neuronal markers (TAU and βIII-tubulin) indicated.

Patient number	Patient 1	Patient 2	Patient 3	Patient 4	Patient 5	Patient 6
Gender (M/F)	F	M	M	F	F	M
Ethnicity	Caucasian (White British)	Caucasian	Caucasian (White British)	Caucasian	Caucasian	Caucasian (White British)
Genetic Infirmation						
(Genome Build)	38	37	38	38		38
gDNA (Genome Build)	16:69320768 A>T	chr16:69354671 A>G	16:69320768 A>T	16:69320768 A>T	16:69320768 A>T	16:69319539G.A
cDNA	c.850A>T	c.850A>G	c.850A>G	c.850A>T	c.850A>T	c.616G>A
Protein (NM_013245.2)	p.Arg284Trp	p.Arg284Gly	p.Arg284Trp	p.Arg284Trp	p.Arg284Trp	p.Glu206Lys
Mutation type	missense	missense	missense	missense	missense	missense
REVEL score	0.97	0.983	0.97	0.97	0.97	0.917
CADD score	35	34	35	35	35	34
Inheritance	de novo	de novo	de novo	de novo	de novo	de novo
Analysis method	WGS	WES/WGS	WGS	WGS	WES	WGS
Clinical Information						
Age at last examination (y or m)	2 y	29 y	2 y	6 m	6 y	
Deceased (age)	no	yes (29 y)	yes (26 m)		no	no
Cause of death		respiratory failure complicating pneumonia	bowel ischaemia and volvulus			
Neurologic						
Intellectual disability (IQ or severity)	severe	severe	severe	severe	severe	severe
Developmental delay	severe	severe	severe	severe poor head control	severe	severe
Motor delay	yes	severe	severe		yes	yes
Speech delay	yes	severe	absent		yes	absent
Epilepsy	no	yes	no	yes	no	yes
Hypotonia	yes	yes	yes	yes	yes	no
Spasticity	mild in upper limbs	yes	yes		no	yes
Ataxia	yes	not assessed - severe motor delay	no		non-ambulatory; dysmetria	no
Dystonia	yes profound	yes	yes	yes	no	no
Other abnormal movements	no	no	chorea		no	no
Sleep disturbances	yes	yes	unknown		yes; central sleep apnea	yes
Brain imaging						
Major features	hypoplastic cerebellar vermis and hemispheres	cerebellar hypoplasia	bilateral polymicrogyria and pontocerebellar hypoplasia	pontocerebellar hypoplasia	progressive pontocerebellar atrophy involving vermis and hemispheres;	severe cerebral atrophy on CT at 1 year
Other MRI findings	thin corpus callosum	corpus callosum hypolasia	follow - up MRI parenchymal loss and possible dysmyelination		decereased cerebral white matter volume with preiventriculat gliosis	
Growth Parameters						
Delivery (wks+days)	37	39	40	38+6	33	38+4
Weight at birth (gr; SD or centile)	2310 g (Z -2.8)	3120 g (25th)		2450 g (Z -2.4)	2083 g (50th-75th)	2073 g (<0.04th)
Length at birth (cm; centile)		48 cm (9-25th)			45 cm (75th)	
Head circumference at birth (cm; SD or centile)	31.4 cm (Z -2.6)	35 cm (50th)		30.5 cm (<0.04th, Z< -3)	25 cm (<0.04th, Z<-3)	31 cm (0.04th-2nd)
Microcephaly	yes	yes	yes	yes	yes	yes
Height (cm; SD)	74.5 cm (Z -1.87)	115 cm (Z -5.5)	78 cm (at 26m) (Z -3.0)		124 cm (Z 1.4)	
Head circumference (cm; SD or centile)		46 cm (Z -6.8)	42 cm (at 26m) (Z -4.5)	39 cm (at 6 m) (Z -5)	42.3 cm (<< 0.04th)	46 cm (Z -5.0)
Weight (kg; SD)	7.645 kg (Z -2.31)	15 kg (Z -6.0)	12.45 kg (at 26m) (Z -0.41)	6.56 kg (at 6 m) (Z -1.1)	21.3 kg (Z 0.17)	2nd-9th centiles
Feeding difficulties	yes - severe gastroesophageal reflux	yes	yes		yes - gastroeosophageal reflux	no
Nasogastric (NG) feeding or percutaneous endoscopic gastrostomy (PEG)	NG/PEG-J	no (declined)	PEG/ fundoplication and jejunal tube		yes	no
Eye phenotype						
Congenital Cataract	yes	yes	yes	no	no	yes
Retinal Dystrophy	yes	no	salt and pepper retinitis		no	yes
Leber congenital amaurosis	no	no	no		yes	no
Vision	no fixing or following	poor fixing and no following	no fix and following	poor fixing and following at 6 m	diminished	diminished
Staphyloma		yes	no		no	
Aphakia	yes (post-operative)	no	no		no	yes
Liver function						
Hepatomegaly	yes and conjugated bilirubinaemia at 1 yr	mild hepatosplenomegaly	progressive hepatomegaly from 1 year of age		congenital hepatosplenomegaly	no
Other	raised AFP	no	haemosiderosis		mild cholestasis, iron overload secondary to CDA-1	
Gallstones	no	yes	microvesicular steatosis		no	no
Musculoskeletal anomalies						
Lipodystrophy	no	yes	no		no	no
Abnormal CPK	no	yes mild on 3 occasions	yes on 2 occasions		not done	no
Muscle biopsy	no	no	myopathic		no	no
Scoliosis	no	yes, severe	no		no	yes
Toe abnormalities		II toes hypoplasia	no	short toes	no	
Hip dysplasia	no	yes	no		coxa valga	yes
Single palmar creases	no	yes	no		no	no
Talipes (bilateral)	no	yes	no	yes	no	yes
Haematological anomalies						
Anemia	yes- raised reticulocyte count and platelets blood film - anisopoikilocytosis	macrocytic anemia with anisopoikilocytosis	no		yes	no
Hemolytic crisis	no	yes	no		no	no
Bone marrow biopsy/aspiration	no	dyserythropoiesis	no - normal at post mortem		no	no
Congenital dyserythropoitic anaemia		yes	no		yes	no
Other features						
Renal defects	no	no	no		no	no
Liver fibrosis	no	no	no		no	no
Sensorineural deafness	no	yes	no		yes	no
Hypogonadism	no	yes	no		no	no
Stipsis	no	yes	yes		yes	no
Stomatitis	no	yes	no		no	no
Dental anomalies	no	yes	no		no	no (delayed eruption)
Recurrent infections	no	yes	no		no	no
Aphakia	post operative	no	no		no	yes
Other comments						left testicular torsion and right undescended testis

Table S1. Genetic and clinical features of patients with de novo heterozygous VPS4A sequence alterations.